UNIVERSITY OF CALIFORNIA, SAN DIEGO

**A Physically-Based Reflectance Model For Mammalian Fur Fibers
Based On Anatomy And Gonioreflectometry Measurements**

A thesis submitted in partial satisfaction of the
requirements for the degree
Master of Science

in

Computer Science

by

Chiwei Tseng

Committee in charge:

    Professor Ravi Ramamoorthi, Chair
    Professor Henrik Wann Jensen
    Professor Jürgen P. Schulze

2015

The thesis of Chiwei Tseng is approved, and it is acceptable in quality and form for publication on microfilm and electronically:

_____

_____

_____

Chair

University of California, San Diego

2015

DEDICATION

To the Sunflower Student Movement.

EPIGRAPH

No cat out of its first fur was ever deceived by appearances,

unlike human beings, who seem to enjoy it.

—Peter S. Beagle

TABLE OF CONTENTS

LIST OF FIGURES

LIST OF TABLES

ACKNOWLEDGEMENTS

Furthermore, I would like to acknowledge my undergraduate advisors, Yung-Yu Chuang and Yuan-Chung Cheng at National Taiwan University. They have taught me well on doing research respectively in the fields of engineering and natural science.

Lastly, thanks to all the past and current group members in the Graphics and Vision Lab for a wonderful year — Krishna Mullia, Muhammad Ahmed Riaz, Matteo Mannino, Ailie Fraser, Jong-Chyi Su, Zachary Murez, Hiroaki Ebi, Sam Iljung Kwak, Oscar Beijbom, Mohammad Moghimi and Jannik Boll Neilsen. Thanks to Yu-Hsien Hwang Fu and my family for all the love and support. Without them, I could not go far.

VITA

2012   B. S. in Chemistry, National Taiwan University

2012   B. S. in Computer Science & Information Engineering, National Taiwan University

2015   M. S. in Computer Science, University of California, San Diego

ABSTRACT OF THE THESIS

**A Physically-Based Reflectance Model For Mammalian Fur Fibers
Based On Anatomy And Gonioreflectometry Measurements**

by

Chiwei Tseng

Master of Science in Computer Science

University of California, San Diego, 2015

Professor Ravi Ramamoorthi, Chair

Rendering photo-realistic animal fur is of practical importance in many computer graphics applications. In the past, the visual appearance of specific fiber types have been studied, and various reflectance models have been proposed. These models, however, lack either physical accuracy or versatility to produce the wide range of specular and diffusive material properties observed on animal fur fibers in the wild. To uncover the cause of various reflectance phenomena in fur fibers, we make two-dimensional far-field reflectance profile measurements on fur fibers from nine mammalian species and a human hair. Based on the measurements, we reconstruct light paths for all the observed re-

flectance lobes and devise a physically-based reflectance model for arbitrary mammalian fur fibers. In our model, a fur fiber is represented by two coaxial cylinder volumes, where an outer cylinder represents the biological observation of a cortex covered by multiple layers of cuticle scale, and an inner cylinder represents the scattering interior structure known as the medulla. By running Monte Carlo simulations, we validate that our model preserves high fidelity to actual animal fur and can simulate a large array of microscopic and macroscopic reflectance phenomena. Finally, we develop a practical, near-field shading approach, based on an analysis in scattering paths over the two-dimensional cross section of the coaxial cylinder model. For efficient rendering, we factor reflectance lobes into separated azimuthal and longituidinal profiles, and include a precomputed component for medulla scattering. We verify the accuracy of our approximation scheme, and show that our practical shading model fits the measurement data significantly better than any prior model, and is capable of capturing many characteristic visual features of real fur fibers.

Chapter 1

Introduction

Animal Fur has very complicated appearance. For animation, game and visual effect studios which utilize modern three-dimensional computer graphics technology as their primary production pipeline, generating photo-realistic images of fur that grows from the skin of the characters has become one of the recurring challenges. Many aspects of fur, including its geometry, dynamics and shading, needs to be studied and modeled carefully in order to produce believable renders.

The complexity in simulating fur appearance with computers arises due to the presence of a large number of cylindrical objects. They collectively contribute to many macroscopic behaviors of fur, which human eyes are sensitive to. Fortunately, the computational power on a modern machine allows explicit representation of fur up to the resolution of a single fiber. Therefore, setting aside efficiency issues, it is often possible to simulate many characteristic features of fur by modeling the properties of each fiber individually and assembling them together in a scene.

In terms of characterizing how a single fiber interacts with light, it is useful to perform analysis in the space of the bidirectional curve scattering distribution function (BCSDF, or f_s). Using radiometric terminology, a BCSDF is a function which encodes,

per unit length of fiber, the ratio of the irradiance from an incident angle to the radiance toward an exiting angle.

$$L_o(\omega_o) = \int_\Omega L_i(\omega_i) f_s(\omega_i, \omega_o) \cos(\theta_i) \, d\omega_i, \tag{1.1}$$

where L is the radiance, ω is the solid angle parameterized over longitudinal and azimuthal angles (θ, ϕ), and the subscripts i and o respectively specify the incident and exiting terms.

The BCSDF is essentially a per-length analogy to the per-area bidirectional scattering distribution function (BSDF). For cylindrical geometry, a BCSDF can be regarded as a BSDF pre-integrated over the width of the fiber. The BCSDF of a fiber does not capture scattering variation for light rays that hit or leave the fiber over the width of the fiber. Therefore, it is relevant to the appearance of a fiber only at a macroscopic level. In practice, we can simply assume a uniform profile over the width of the fiber. This approximation scheme is commonly known as the *far-field approximation*. The far-field approximation is the fundamental assumption behind much prior work in rendering photo-realistic fibers, and is deemed adequate for scenes where the width of a fiber never spans across multiple pixels.

Seminal work in modeling the macroscopic appearance of a batch of fine cylindrical objects is done by Kajiya and Kay [KK89]. They develop a phenomenological reflectance model for fur by considering cylinders that exhibit Lambertian and Phong reflections, which leads to a diffuse component depending on the longitudinal angle of the incident light and a specular component producing a cone of highlight (Figure 1.1). In terms of BCSDF, they arrive at

$$f_s(\omega_i, \omega_o) = k_d + k_s \frac{\max\left[\cos^p(\theta_i + \theta_o), 0\right]}{\cos(\theta_i)}, \tag{1.2}$$
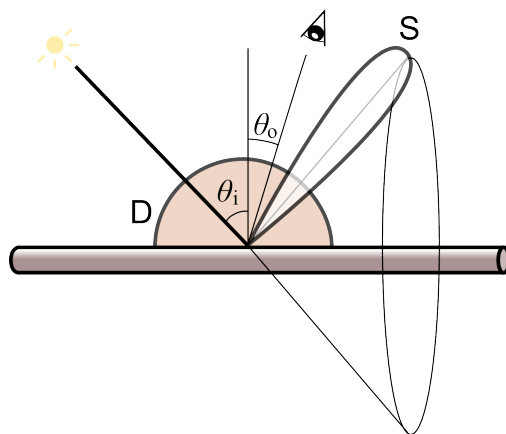
Figure 1.1: The Kajiya-Kay model.

where k_d is the diffuse reflectance, k_s is the specular reflectance, and p is the Phong exponent for the sharpness of the highlight. The model successfully captures an elongated shape for specular highlight that has been observed commonly on fur and hair, which readily arises from the cylindrical geometry of a fiber. Nevertheless, the model is not energy conserving, which makes it incompatible for physically-based light transport algorithms. Additionally, it is not capable of simulating the appearance of a translucent fiber, and is unrealistic in a way that the model is azimuth-independent.

Unlike the Kajiya-Kay model, which is empirically derived based on simple geometry, more recent work focuses on approximating the appearance of more specific classes of real-world fibers. Indeed, much of the attention has been drawn toward developing models and algorithms for rendering photo-realistic human hair, due to its ubiquity in computer games and animated film. [MJC$^+$03] measure the one-dimensional reflectance profiles of real, translucent human hair fibers and develop a shading model composed of surface (primary) reflection, transmission, and internal (secondary) reflection components. These components are denoted respectively as the R, TT and TRT components according to their scattering paths, where each R indicates a reflection event and T a transmission (or refraction) event (Figure 1.2).

The Marschner Model is generally recognized as a physically-based model for
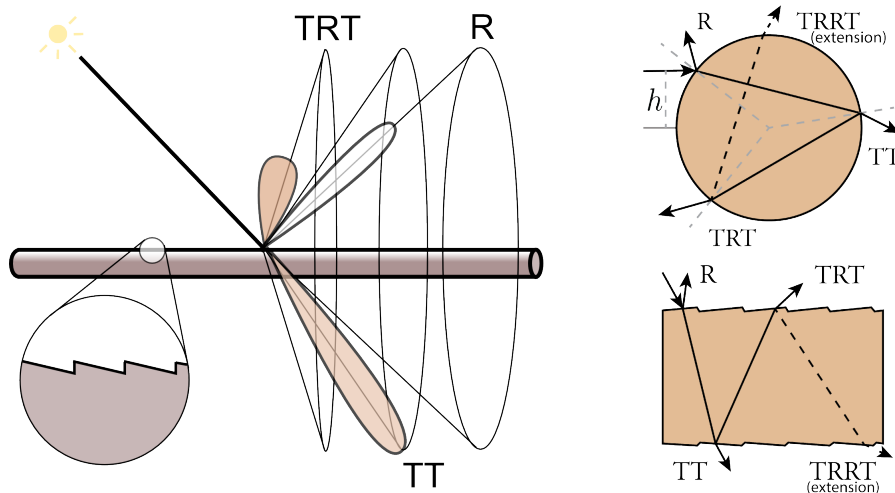
Figure 1.2: Illustration of the Marschner human hair model and all scattering paths (including d'Eon's extension) it considers.

human hair fiber. Their work straightforwardly relates the reflectance features captured in their measurement data to the microscopic geometry of a human hair fiber. Specifically, they approximated each fiber as a rough elliptical dielectric cylinder. To model the scales that cover the human hair shaft, the surface normals of a cylinder are modified to tilt systematically toward the root of the hair. The tilt offsets the specular highlight for each component to peak at a different angle. As for the volume of the cylinder, a homogeneous absorptive medium is considered, modeling pigments in the human hair shaft. The Marschner model produces scattering patterns that match significantly better than the Kajiya and Kay model to reference photographs of human hair.

Although the Marshcner model generates visually accurate appearance of human hair fibers, several issues remain.

- It lacks some reflectance features observed on real hair fibers, notably diffuse reflectance. On fitting the Marschner model to photographs of human hair, [ZRL+09] discover that, by adding an ad-hoc Lambertian diffuse component to the Marschner model, the fitting quality improves significantly. [dFH+11] make an attempt to resolve this issue. They make physical corrections to and generalize the Marschner

model to include higher-order scattering paths which leads to additional lobes such as the *TRRT* component. However, their energy analysis suggests that these components are not the cause to diffuse reflectance in a hair fiber.

- Its governing parameters are physically-based, which are inconvenient for art-direction and cannot produce quasi-physical but photo-realistic appearances. [SPJT10] resolve this issue by factoring the Marschner model (with dual scattering approximation by [ZYWK08]) into a set of lobes which are more intuitive and controllable for artists.

- It addresses only the far-field profile of hair fibers. Since this issue arises from the BCSDF framework itself, [ZW07] propose an eight-dimensional bidirectional distribution function to include the near-field scattering effects. The function is called the bidirectional fiber scattering distribution function (BFSDF), which is essentially a bidirectional scattering-surface reflectance distribution function (BSSRDF) over an enclosing cylinder of the fiber.

These extensions largely strengthen the capability, physical accuracy and consistency of the Marschner model. However, there is a shared caveat in all these models — none of them investigate how the subsurface structures within a hair fiber may drastically affect the macroscopic appearance of the fiber.

In contrast to human hair fibers, the reflectance of animal fur fibers has not been specifically studied in the field of computer graphics. Regarding biological homology, one may naturally assume that any animal fur fiber is sufficiently similar to a human hair fiber in terms of optical properties, and thus can be rendered using a scattering model developed for human hair fibers. This assumption, however, is found to be inadequate, as briefly reported in [dFH+11]. The general qualitative consensus is that an animal fur fiber can appear to be much rougher and more diffusive than a human hair fiber.

Figure 1.3: Appearance of various fur fibers.

The visual characteristics between fur fibers from two species can differ significantly. In Figure 1.3 we show several photographs to exemplify the diversity in appearance of fur. Additionally, it is crucial to acknowledge the fact that a human hair fiber actually *is* an animal fur fiber. From this perspective, animal fur, as a class of fiber, easily spans a much wider perceptual space in appearance than what the Marschner model and its many extensions can produce. As a result, versatility becomes critical to a reflectance model designed for *any* animal fur fiber. To become useful, the scattering model should be capable of approximating all the points in the perceptual space of fur, including the points in the already well-studied subspace of human hair.

The goal of our work is thus to first resolve a scattering theory for fur that accounts for all the scattering mechanisms within a fur fiber. We then aim at forming a practical, versatile and sufficiently simple shading model by deriving either analytic or numerical approximations to the scattering theory.

The organization of the thesis is now given. We first present an anatomy of a mammalian fur fiber and suggest links between their microscopic structures and macro-

scopic reflectance features. In need for stronger evidences that support these links, we build up the first database in computer graphics of two-dimensional far-field reflectance data acquired from nine mammalian fiber samples and a human hair sample. Based on our measurements, we form a scattering theory for fur fibers. We then accordingly devise a novel reflectance model for fur fibers and with which, we run three-dimension light transport simulations. We fit our reflectance model to the measurement data and achieve close quantitative match between the synthetic and acquired two-dimensional reflectance profiles. Upon the establishment of our reflectance model, we develop a practical and accurate near-field shading approach, considering factorization and precomputation of reflectance profiles. Finally, we show synthetic images generated with our practical shading approach and revisit prior work in hair shading to support them with clearer physical pictures according to our result.

Chapter 2

Fur Fibers

2.1 Anatomy

We now give a brief overview on the structure of an animal fur fiber, summarizing literature from other fields, [DK04a], [DK04b], [CH11], [GGKGJ11] and [Has88]. We start by elaborating the structure of a human hair fiber, and then generalize to common mammalian fur fibers.

The shape of a human hair shaft is roughly an elliptical cylinder. It is mainly composed of protein (mostly keratin filaments) and biologically inactive cells. Depending on the moisture content, protein comprises approximately 65% to 95% by weight of a human hair shaft [Rob12]. It is evident that a hair fiber is dielectric.

A human hair shaft is composed of three concentric parts — cuticle, cortex and medulla — from the outermost to the innermost. *Cuticle* consists of flat cells that partially overlaps with each other like roof shingles, covering the surface of the hair shaft and make its normal tilted systematically toward the root of the hair. Each cuticle scale is composed of two electron-dense outer layers called A-layer and exocuticle, and an inner layer of organelle debris called endocuticle. Multiple cuticle scales can stack up and
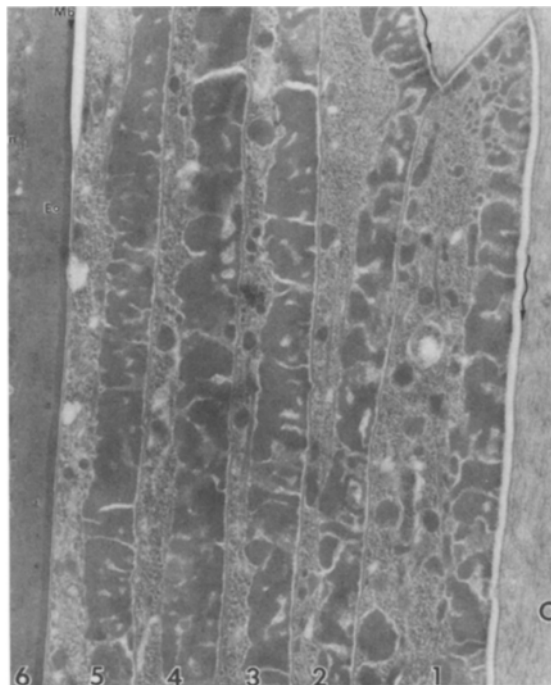
Figure 2.1: A slice of cuticle scales on human hair shaft. Image courtesy of [Has88].
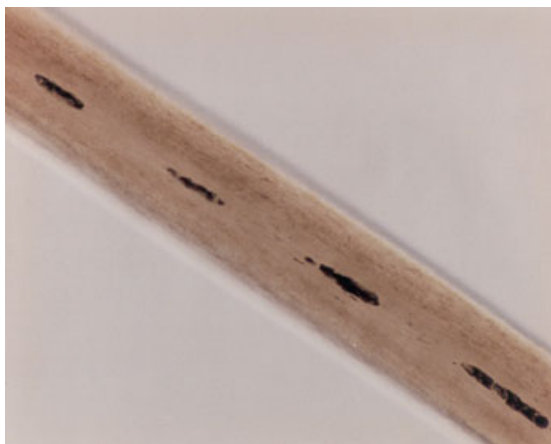
Figure 2.2: Bright-field microscopy image of a sample of human hair fiber. Image courtesy of [DK04a].
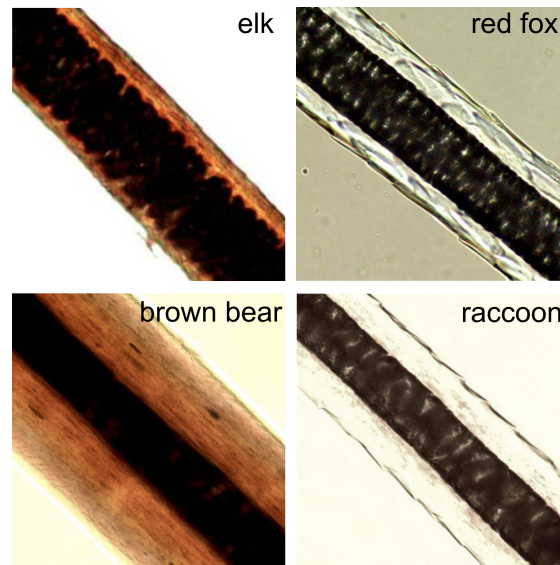
Figure 2.3: Bright field microscopy images of various animal fur fibers. Images courtesy of [CH11].

form a structure of multiple layers over the surface (Figure 2.1). *Cortex* is the thickest, and the most homogeneous layer in human hair shaft, where keratin filaments bundle together to form dense and organized super-coiled strands. This zone may contain an abundant amount of melanin pigments such as eumelanin or pheomelanin, both of which have high absorptive coefficients for light. Different concentrations of eumelanin give colors to blonde, brown and black hair, while additional pheomelanin makes them appear red. *Medulla* is an open and unstructured zone at the core of a hair shaft. It may or may not be rich in pigments like cortex, but contains hollow granules and vacuoles among disorganized keratin filaments. In a human hair shaft, it can be small, interrupted, fragmented or even absent. An optical microscopy image of a human hair fiber is shown in Figure 2.2.

For fur fibers besides human hair, cuticle, cortex and medulla are generally present. Additionally, each of the three parts is also relatively consistent in structure between animal species. However, as shown in Figure 2.3, there exists certain prominent variations among fur fibers across multiple species, which can be observed directly under

an optical microscope.

Cuticle. While a human hair shaft has cuticle scales that resemble roof shingles, cuticles on a fur fiber from other mammalian species can have very complex surface geometry. Commonly observed scale patterns include lattice, petal-like and tile-like patterns, which can be observed with scale-casting techniques in forensic science. Additionally, cuticle scales can overlap each other to different extents, covering the cortex with multiple layers of coating with various thickness and roughness.

Cortex. The cortical volume of a fur fiber may have an abundant concentration of melanin pigment, as in a human hair fiber. The variation in pigment concentration primarily contributes to the different colors of fur. Besides pigments, cortex also contains varying concentrations and distributions of organelles like ovoid bodies and cortical fusi.

Medulla. The *medullary index* of a fur fiber is defined as the ratio of the diameter of the medulla to that of the fiber. Human hair fibers generally have medullary indices below 0.33, while fur fibers from other mammals fall between 0.5 to 0.9. The shape and distribution of granules and vacuoles within the medulla vary between species. In addition, a medulla can be naturally or artificially filled with mounting media besides air, such as water or Canada balsam.

2.2 Optical Properties

All animal fur fibers are mainly composed of keratin. [HLLS11] establish the refractive index of keratin from bird to be between 1.54 to 1.58 under visible light. [SGF77a] report an effective refractive index of 1.55 on human hair fiber. We assume that the refractive indices for common mammalian fur fibers are close to these values.

A Fur fiber is translucent when the concentration of pigment is low within its volume. From the bright field optical microscopy images shown in Figure 2.3, one can observe very clearly that most fur fibers are far from homogeneous, and that the medulla always appears much darker than the cortex. Moreover, depending on the structures within the medulla volumes, a different amount of light is transmitted through the medullas. Evidently, there exists a discontinuity in extinction coefficients over the medulla surface, where the medulla volume is at the higher end of the discontinuity. High extinction coefficients for the medulla volume is further supported by scanning electron microscopy (SEM) images over the the cross section of a fur fiber [GGKGJ11], where one can observe the drastic fluctuation of electron density within the medulla, providing an environment for lots of dielectric scattering events.

For a human hair fiber, we have mentioned that it is special for having a much smaller medulla than any common mammalian fur fiber. Therefore, its appearance under a microscope closely resembles a homogeneous dielectric cylinder. This observation directly justify why the Marschner model is applicable to human hair fibers, but not generally applicable to *any* fur fiber. However, note that although the medulla is small and fragmented in a human hair fiber, the discontinuity in volumetric scattering property still exists and can affect the reflectance features of the fiber.

Besides bright field optical microscopy, many other microscopy techniques also provide helpful information about the optical properties of a fur fiber. The *dark field microscopy* is an optical microscopy tool where the light source does not directly face the observer. Therefore it only resolves light being scattered by the specimen. In an image of a fur fiber captured under a dark field microscope, as seen in [DU03], the medulla generally scatters much more light than the cortex, which again implies its high scattering coefficient. Interestingly, the scattering signal does not merely come from the medulla, but also from the very thin cuticle layer close to the surface of the fiber. This suggests

that the cuticle is, in addition to the medulla, another structural component that scatters light prominently in a fur fiber.

To the best of our knowledge, no prior work has established how medulla and cuticle contribute to the macroscopic appearance of a fur fiber. However, in the field of cosmetic science, it is well understood that the presence of a porous medulla in a human hair fiber will make it appears lusterless [NSA$^+$02b] [NSA$^+$02a], and that of a healthy cuticle will generate the most glittering speckles over the fiber surface [OYM$^+$03]. Based on goniophotometric measurements, [SGF77a] and [SGF77b] propose arguably the earliest reflectance model for human hair, where they address the surface reflectance and specific scattering lobes from a hair fiber to the cuticle and an underneath layer with low electron density. High scattering coefficients for the medulla and low ones for the cortex in human hair fibers are experimentally established by [KVVU09].

To sum up, microscopy images of fur fibers and prior studies in human hair appearance both emphasize the importance of the cuticle and the medulla to the macroscopic appearance of an animal fur fiber. Despite that the optical properties for each part of a fur fiber is somewhat established, how they affect the overall reflectance profile of a fur fiber remains vague and unclear. We resolve this question in the next chapter by acquiring two-dimensional far-field reflectnace profiles of fur samples from various animal species.

Chapter 3

Gonioreflectometry Measurements

3.1   Acquisition Framework

None of the prior studies ha related the macroscopic visual properties of a fur fiber to its cuticle and medulla, and for human hair fiber, none as directly as from the BCSDF domain. In order to resolve the influences of cuticle and medulla, we make the first two-dimensional far-field reflectance profile measurements on fur fibers in the field of computer graphics.

All the far-field reflectance profiles measured in the thesis are acquired using the UC San Diego Spherical Gantry (Figure 3.1). The gantry has two robotic arms, on which a light bulb and a charge-coupled device (CCD) sensor are respectively attached. Each of the arms can be controlled in the longitudinal and azimuthal degree-of-freedoms. The camera arm records the radiance at different directions, 3 feet away from the sample, and the light arm illuminates the sample at various incident directions, 2 feet away from the sample. We utilize a 150-watt quartz halogen bulb as the light source (Dolan-Jenner DC950 Illuminator) and a digital camera with 35 mm lens (Point Grey Scorpion Digital Camera) as the sensor. Although red, green and blue channels are all recorded, we merge
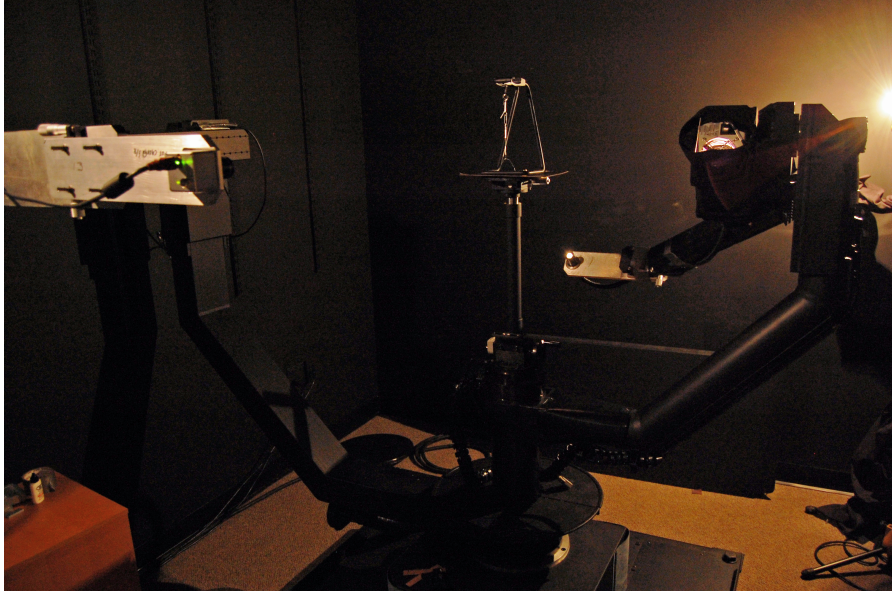
Figure 3.1: The UC San Diego Spherical Gantry.

the channels by averaging them into a single intensity image so as to focus only on the scattering pattern.

In these reflectance measurements, a single fur fiber is hung on a hair stand and straightened by gravity with weights. The incident and exiting directions are parameterized in azimuthal (ϕ) and longitudinal (θ) angles, where we let $\phi = 0°$ be the incident plane of light and $\theta = 0°$ be the normal plane of the fiber. The root of the fur fiber is at the top, corresponding to $\theta = 90°$, and the tip is at the bottom, where $\theta = -90°$. Note that this parameterization is the same as the coordinate system used in [MJC$^+$03], but with θ flipped. Figure 3.2 shows the measurement settings and the parameterization.

We fix the light source at $(\phi, \theta) = (0°, -40°)$, and capture images with the sensor sweeping over $\phi \in [-20°, 200°]$ at $5°$ steps and $\theta \in [10°, 50°]$ at $2°$ steps. The swept range covers all the specular and diffusive scattering lobes introduced in prior human hair scattering models, but only spans across a quarter-sphere for efficiency reasons. In other words, we implicitly assume that the fur fiber is symmetric over the incident plane. To ensure the validity of this assumption, we calibrate the fiber before each
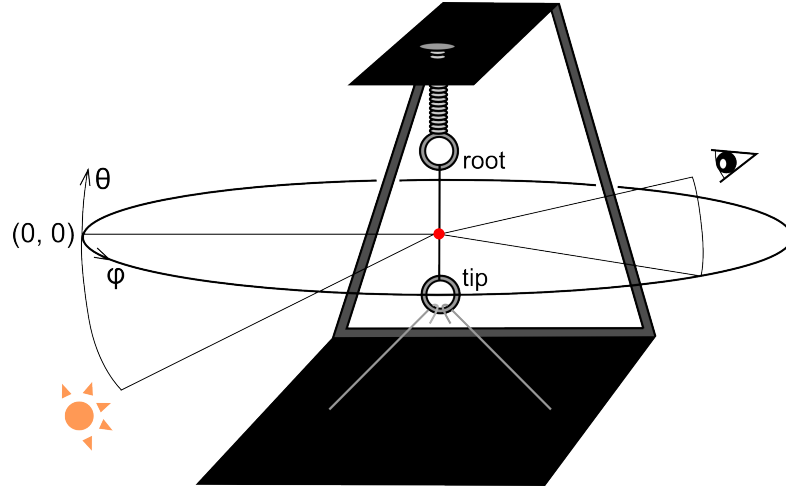
Figure 3.2: Settings for two-dimensional far-field scattering profile measurements.

set of two-dimensional measurements by rotating it along its tangent direction until a qualitatively symmetric one-dimensional normal plane scattering profile is captured. If such symmetry in scattering pattern is never observed on a fur fiber, we simply dispose of the sample.

For each direction, we capture five images for each of five stops in shutter speed. (25 images is captured in total.) Each image is first cropped to a 25-by-25-pixel patch which contains the fiber. Then, the five patches for each shutter speed are averaged over to eliminate temporal noise. Next, we leverage the five averaged patches under different shutter speeds to construct a point in the high dynamic range reflectance profile we intend to resolve. Following the radiance reconstruction algorithm by [DM97], we find that the response function of our CCD sensor is almost perfectly linear within the middle 80% of the dynamic range. Hence, we simply select the one patch from the five which contains the highest number of pixels that lie within the linear range of the response function. Finally, we sum over all the pixels in the selected patch and scale the sum according to the shutter speed to obtain a value of reflectance intensity.

3.2 Reflectance Database and Theory

Under the measurement settings described in the previous section, we build up a database of two-dimensional far-field reflectance profiles of fur fibers from nine different animal species. The nine species are bobcat, cat, deer, dog, mouse, springbok, rabbit, raccoon and red fox. We also measure the reflectance profile of a human hair fiber for comparison and for verification against data from prior work. For our purpose of investigating all possible scattering patterns from fur fibers, we do not focus on the taxonomic details; the names of the species are only for reference. However, we assume that the ten samples (including a human hair fiber) span a sufficiently large space in the BCSDF domain that includes the most important scattering phenomena from common fur fibers [1].

The entire database is displayed in Figure 3.4. We also show in Figure 3.3 the synthetic two-dimensional far-field reflectance profile of a rough homogeneous dielectric cylinder, generated with Monte Carlo simulation. It is easy to notice significant inconsistencies between the two-dimensional far-field scattering profiles we acquire and the one we synthesize. The major inconsistencies are as follow.

- The reflectance profile from a fur fiber may have a blurry and partly occluded TT component around $\phi = 180°$ (mouse and raccoon) or even an absent TT component (cat). Note especially the sharp edge where TT vanishes for the raccoon fur sample. Additionally, the TRT component may become dimmed (mouse) or absent (cat). The original TT lobe may also get replaced by a more diffusive lobe at the same outgoing direction (dog, rabbit).

- The R component in a reflectance profile of a fur fiber is usually extremely bright and blurry, and thus cannot be explained with Fresnel reflection alone (dog, mouse,

---

[1]To be precise, the reflectance profile is proportional to the BCSDF multiplied by a $\cos\theta_o$ factor.
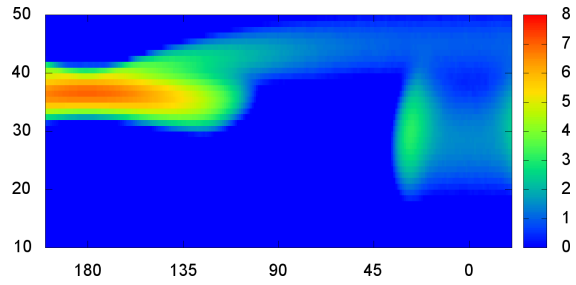
Figure 3.3: Synthetic two-dimensional far-field reflectance profile of a rough homogeneous dielectric cylinder.
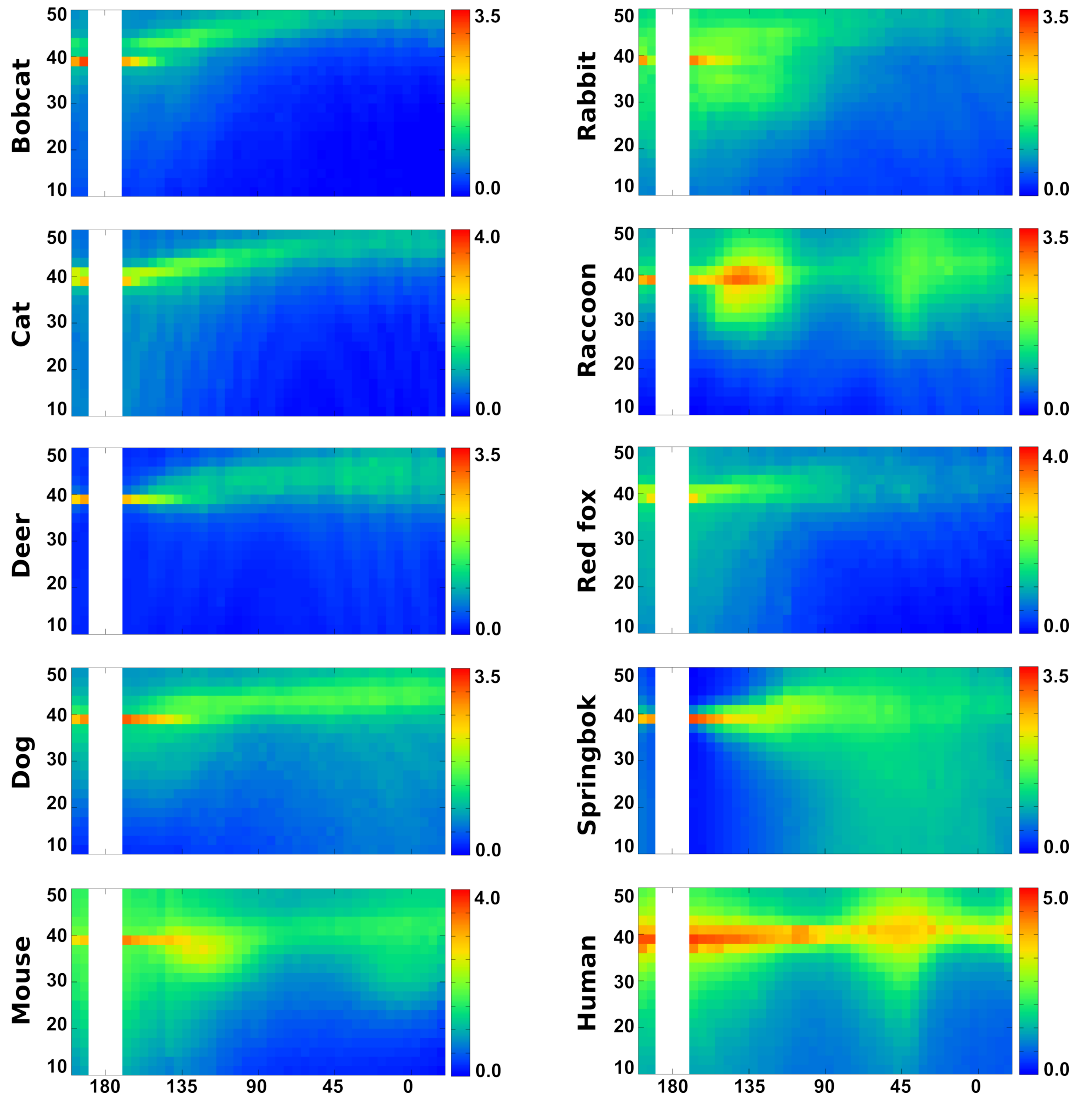
Figure 3.4: The fur reflectance database: two-dimensional far-field reflectance profiles for nine mammalian fur samples and a human hair sample. The signals are radiance in arbitrary units and displayed in logarithmic space to visualize perceptual brightness

raccoon and springbok).

- Many reflectance profiles resolve stripes. These stripes are symmetric over the forward and the backward halves of a reflectance profile.

- Forward and/or backward diffuse lobes appear in many reflectance profiles. The centers of the lobes mostly lie on the normal plane ($\theta = 0°$).

These inconsistencies directly indicate that it is improper to utilize the Marschner model, which only considers a homogeneous dielectric cylinder, to shade an arbitrary fur fiber.

We need to form a new scattering theory based on our understanding about animal fur. Forming the theory is an iterative process that involves many turns of making and validating hypothesis. Since it is challenging for us to experimentally modify the optical properties of a fur fiber, we resort to thought experiments for validation. Fortunately, given all the information about fur fibers discussed throughout Chapter 2, it has become relatively straightforward to trace an imaginary ray of light through the system and figure out the potential scattering events. We have already established in Chapter 2 that the medulla and the cuticle are the dominant parts which scatter light. Thus, what remains is to figure out which of the two components is responsible for the observed inconsistencies.

In an occluded TT component, the supposedly contributing light must have been scattered away or blocked by the cuticle or the medulla. From the partly occluded cases, such as the profile of a raccoon hair, the TT components are only blocked at around $\phi = 180°$. Moreover, the edges of the shadow are sharp. Since the cuticle scales are over the surface of a fur fiber, they do not bring about any discontinuity that can cause such partial occlusions and sharp shadow boundaries. Hence, the TT occlusions can only be explained by the medulla. The deduction for TRT occlusions naturally follows suit, since a TRT path is merely a two-fold extension to a TT path. Also, since the medulla of a
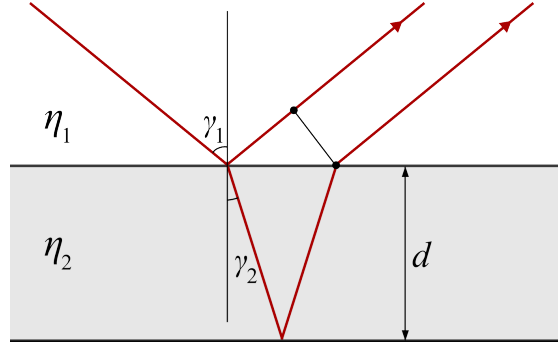
Figure 3.5: Notations used in optical path analysis for thin-film interference.

fiber can get filled with a different dielectric material from the cortex, the presence of the cortex-medulla interface introduces new reflection and refraction events, giving rise to new lobes. For instance, the primary reflection off the cortex-medulla interface should roughly resembles the shape of the R lobe, since both of them are formed by reflection over a cylindrical object, and yet should be tilted to the same longitudinal angle as a TT lobe, as their scattering paths both interact with the inclined cuticle scales twice.

Light in the R component interacts with the fiber merely over the surface. There-fore, the bright and blurry R components we observe can only be explained by the cuticle scales. Indeed, the cuticle is composed of multiple overlapping dielectric layers, as shown in Figure 2.1, which can easily boost up the Fresnel reflectance and the apparent roughness of the surface. We further consider the stripes resolved in many of our scatter-ing profiles. It is very likely that these stripes are due to thin-film interference over the cuticle layer. Following the hypothesis, an analysis in optical path distance leads to the below criterion for constructive interference (Figure 3.5).

$$2\eta_2 d\cos\gamma_2 = \left(n - \frac{1}{2}\right)\lambda, \qquad n \in \mathbb{N} \tag{3.1}$$

where η_2 is the refractive index of the film, d is the thickness of the film, λ is the
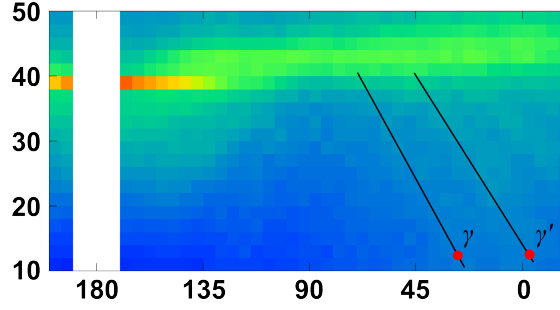
Figure 3.6: Constructive interference fringes in the reflectance profile of a dog hair, and the points we use for optical path analysis.

wavelength of the light, and γ_2 is the refracting angle. According to Snell's law,

$$\theta_2 = \sin^{-1}\left(\frac{\eta_1 \sin \gamma_1}{\eta_2}\right). \tag{3.2}$$

For two consecutive bright fringes in our scattering profile, using equation 3.1, we have

$$2\eta_2 d(\cos\gamma_2' - \cos\gamma_2) = \lambda, \tag{3.3}$$

where γ_2' is defined similarly as γ_2.

$$\gamma_2' = \sin^{-1}\left(\frac{\eta_1 \sin \gamma_1'}{\eta_2}\right). \tag{3.4}$$

We plug in values relevant to our measurement data. For example, we pick the two points shown in Figure 3.6 from the reflectance profile of a dog fur fiber. The incident angle of light at the two points we pick are respectively $\gamma_1' = 25.7°$ and $\gamma_1 = 32.4°$. We further let $\eta_1 = 1.0$, $\eta_2 = 1.55$ and $\lambda = 550$ nm to approximate our measurement settings. The obtained thickness of the cuticle layer, d, is at around 8 μm. This value conforms in magnitude to the thickness of the cuticle layer in a dog fur fiber, 1.8 μm–8.3 μm, as reported by [SMKK06]. As such, we have shown that there exists at least one additional dielectric interface (presumably the cuticle-cortex interface) below the fiber surface that

is important to the macroscopic appearance of a fur fiber.[2] Note that, as early as in 1977, [SGF77a] have already included this interface in their reflectance model for human hair fiber.

Finally, we need to address the forward and backward diffuse lobes. These lobes mostly lie on the normal plane in our profiles. Since they retain very little directional information, it is likely that they arise from light that undergoes a series of scattering events. Scattering from cuticle is not likely to achieve this sort of effect, since it is a thin structure which overlaps very shortly with most light paths. Medulla, however, provides a volume filled with randomly distributed dielectric interfaces, and is prone to multiple scattering events. Therefore, we associate the medulla with the forward and backward diffusive lobes. Note that in some cases, for instance, the profiles for mouse and red fox fur samples, we also observe a glow around $(\theta, \phi) = (40°, 180°)$. The glow is contributed by the light that gets scattered by the medulla to a lesser extent, which leaks through the medulla.

We conclude this chapter by summarizing the light scattering theory we form based on the anatomy, the optical properties and the measurement reflectance data of mammalian fur fibers. To describe a scattering path, we denote scattering events on the cuticle with upper-case letters, and that on the medulla surface with lower-case letters, where R and r indicate reflection, while T and t indicate transmission (or refraction).

Cuticle.   The multiple dielectric layers of cuticle scales collectively contribute to the high surface reflectance on a fur fiber. The accumulative roughness from each layer of scales decorates a heavy tail onto the specular R, TT and TRT components. Thin-film interference over the cuticle layer may resolve stripes over the reflectance profile.

---

[2]It is noteworthy, however, that our hypothesis of thin-film interference predicts a slightly different Moiré pattern to what are resolved in the database. Further investigation may be required regarding the inconsistency.
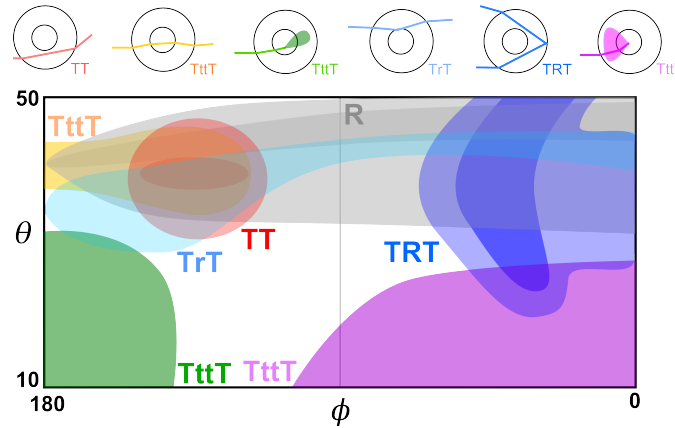
Figure 3.7: A map of all the lobes we observe in the acquired reflectance profiles and their respective scattering paths.

Medulla. Medulla is an inhomogeneous volume of high scattering coefficient. Hence, it may fully or partially scatter the TT and TRT components out of its original path, and produce significant forward or backward diffuse lobes ($TttT$) in the reflectance profile. The medulla can be anisotropic due to the nature of its participating medium, such as the distribution of vacuoles and granules within its volume. It also introduces an additional dielectric interface, that can give rise to extra lobes (TrT).

Figure 3.7 shows a map of all the speuclar and diffuse lobes we observe in our database. We assign to each of the lobes a scattering path that accounts for its formation according to the scattering theory for fur fiber. At this point, we consider the links between the microscopic structures of a fur fiber and its macroscopic appearance concretely resolved. We turn to developing a reflectance model for fur fibers based on our new insights.

Chapter 4

Coaxial Cylinder Model

The light scattering theory for animal fur fibers presented in the previous chapter directly relates the subsurface structure of a fur fiber to its reflectance profile. Although the theory itself is a straightforward result concluded through analyzing the fundamental optical properties of the major parts of a fiber, to model it requires further experiments and simulations. In this chapter, we introduce the *coaxial cylinder model*, a faithful representation of a fur fiber based on the scattering theory formed in Chapter 3. We run three-dimensional light transport simulations to compute synthetic two-dimensional far-field reflectance profiles, with which we fit the coaxial cylinder model to the measurement data. The work we present in this chapter solidly backs up the scattering theory for fur fibers, as well as provides a prototypical model from which which a practical shading model can be developed.

4.1   Components

We consider a fur fiber as an inhomogeneous cylinder with an elliptical cross-section. For the sake of simplicity and practicality of the model, we do not consider fur fibers of other geometry. This assumption does not hold for all types of fur fibers, and
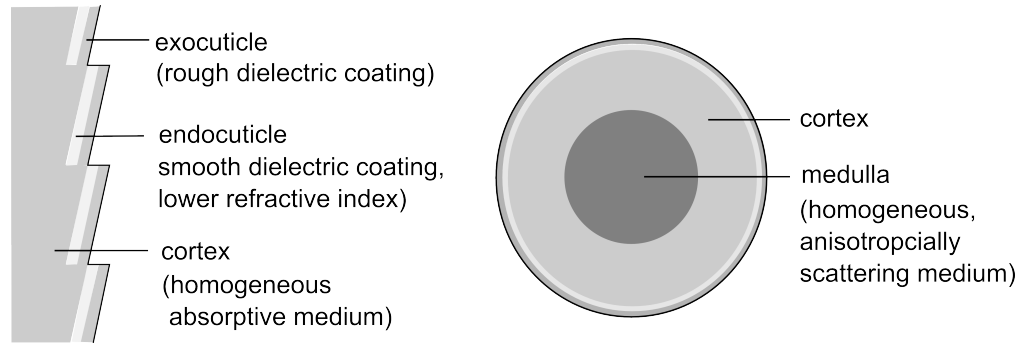
Figure 4.1: The coaxial cylinder model.

should be revisited for fibers known to have more interesting shapes. However, we do not find this assumption restrictive on fitting the coaxial cylinder model to the nine fur samples and a human hair in our database introduced in Chapter 3.

To model the inhomogeneity within a fur fiber, we use explicit geometry to represent cuticle, cortex and medulla in the coaxial cylinder model. In addition to an outermost cylinder that defines the surface of a fur fiber, a total of three coaxial cylinders are utilized to approximate the subsurface structures of a fur fiber, which correspond to the interfaces between exocuticle and endocuticle, endocuticle and cortex, and cortex and medulla. We extract a set of parameters to control the properties of the interfaces and their associate volumes based on what the scattering theory predicts to be the most significant factors that will change the macroscopic appearance of fur.

Interfaces. All the four interfaces are dielectric ones, and we consider roughness only for the outer-most fiber surface. Roughness for the interface is modeled using microfacet theory using Beckmann half-vector distribution [WMLT07]. Since the cuticle scales are systematically tilted toward the root of the fiber, the surface normals for these three interfaces are modified by the same adjustable angular offset. For a fiber with circular cross section, the refractive index of exocuticle and cortex is fixed to 1.55, while that of endocuticle and medulla are left as parameters which must not exceed 1.55. To model

eccentricity, we follow the approximation scheme by [MJC$^+$03] and simply adjust the refractive indices for all the dielectric materials with

$$\eta^* = 2(\eta - 1)a^2 - \eta + 2, \tag{4.1}$$

where η^* is the effective refractive index and a is the eccentricity. This relation is a first-order approximation where the major axis of the elliptical cross section is perpendicular to the incoming light.

It is important to note that the endocuticle layer in our model is only a reduced formulation. In essence, we collapse the multiple layers of cuticle scales into one so as to simplify the model. This simplification, however, does not practically limit the capability of the model. One should regard the refractive index we associate with endocuticle as an effective value. They arise from the collective contributions by both the material and the implicit multi-layer structure. To further simplify the concept of effective refractive index for cuticle, we instead convert the value into an equivalent number of layers of dielectric slabs. We consider each slab being sandwiched by layers of air, and fix the refractive index of the slabs to 1.55. We refer to [Sto60], where the reflectance of one layer of dielectric slab is

$$F(\theta_i; 1) = F(\theta_i) + \frac{[1 - F(\theta_i)]^2 F(\theta_i)}{1 - F^2(\theta_i)}, \tag{4.2}$$

where F is the Fresnel reflectance and θ_i is the incident angle. Considering l layers together, the collective reflectance is then given as

$$F(\theta_i; l) = \frac{l \cdot F(\theta_i, 1)}{1 + (l - 1) \cdot F(\theta_i, 1)}. \tag{4.3}$$

To obtain l from our effective refractive index of cuticle, we make an approximation by

Table 4.1: The list of all parameters for the coaxial cylinder model.

Parameter	Definition
κ	medullary index (rel. radius length)
η_c	refractive index of cortex
η_m	refractive index of medulla
α	scale tilt for cuticle
β	roughness of cuticle (stdev.)
$\sigma_{c,a}$	absorption coefficient in cortex
$\sigma_{m,s}$	scattering coefficient in medulla
g	anisotropy factor of scattering in medulla
l	layers of cuticle scale.

equating $F(0°, l)$ and the total Fresnel reflectance from the three cuticle-related interfaces at $0°$ incident angle, which can be numerically computed. Note that in [Sto60], l is an integer, while we extend it to a real number for continuous parameterization.

Volumes. The volume that represents cortex is purely absorptive, and the volume that represents medulla purely scatters light. How granules and vacuoles are distributed within the medulla volume influences the amount of light getting forward or backward scattered by the medulla. To simulate this effect, We leverage the Heyney-Greenstein phase function to model the scattering anisotropicity using a single parameter g [HG41].

$$p(\theta; g) = \frac{1 - g^2}{4\pi \cdot (1 + g^2 - 2g\cos\theta)^{1.5}}. \tag{4.4}$$

Under natural circumstances, we only consider g to be larger or equal to 0, which corresponds to isotropic or forward volumetric scattering.

A full list of parameters for the coaxial cylinder model is shown in Table 4.1 and Figure 4.1.

4.2   Microscopic Appearance

As a preliminary assessment, we render images with the coaxial cylinder model to show that our proposed model produces realistic appearances matchable to real microscopy photographs of fur fibers. Furthermore, we show that there exists specific visual properties which can be simulated with our scattering model, but are hard to simulate using other scattering models. In all of the following sections and chapters, we utilize Mitsuba [Jak10], a physically-based renderer, to run the light transport simulations.

Since the coaxial cylinder model largely stays true to the anatomy of a real animal fur fiber, it naturally retains the capability of rendering both the microscopic and macroscopic appearances of a fur fiber accurately. To demonstrate the mentioned strength of our model, we prepare a scene that mimics the settings of a fur fiber under a bright field microscope. We then compare the synthetic image to a microscopy photograph captured under a similar environment (Figure 4.2). The synthetic image is rendered with photon mapping.

If a fur sample is prepared on a wet-mounted slide for optical microscopy, the mounting medium may at times get filled into the medulla, in which case the appearance of the medulla changes dramatically. When this happens, the fluctuation of refractive index within the medulla volume reduces significantly, essentially making the volume far more homogeneous. To simulate this effect in the coaxial cylinder model, we simply tune down the scattering coefficient of the medulla volume ($\sigma_{m,s}$).

The degree of inhomogeneity within the medulla volume critically modifies the synthetic appearance of a fur fiber. To our knowledge, this phenomenon cannot be simulated with any other scattering model, but arises readily in the images synthesized with our model, and can be conveniently controlled by simply adjusting the scattering coefficient of the medulla volume. The match suggests our model's high fidelity to its
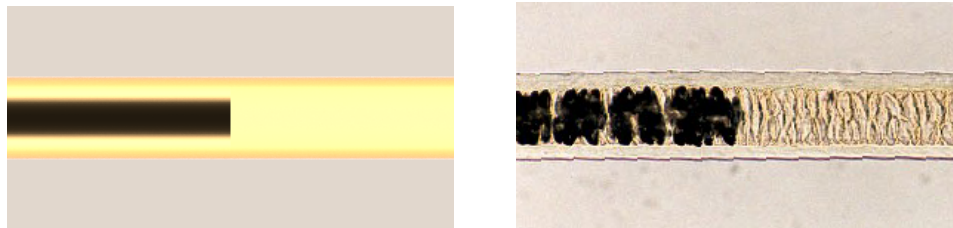
Figure 4.2: Synthetic bright field microscopic appearance of a fur fiber with medulla filled with air or water, and a reference microscopy photography.

real-world counterpart.

4.3   Far-Field Scattering Profile

As stated in Chapter 1, the macroscopic appearance of a fur fiber is directly associated with its far-field reflectance profile, or more precisely, its BCSDF. The two-dimensional far-field reflectance profiles provide a good basis for qualitative and quantitative analysis of scattering characteristics. Although the profiles do not account for near-field scattering effects, it is generally adequate for common applications, since a fur fiber is mostly observed over a distance that is of a larger order of magnitude than its diameter.

We leverage bidirectional path tracing to simulate the reflectance profile of the coaxial cylinder model. In each scene, the centroid of the model is placed at the world origin with its tangent pointing downward. This exactly duplicates the gonioreflectometry measurement settings described in Chapter 3. Using the former spherical parameterization of incident and exiting angles, a rectangular object, with infinitesimal height and with width fixed to the diameter of the fur fiber, uniformly emits collimated light towards the origin from $(\phi, \theta) = (0°, -40°)$. We record the irradiance signal over a sufficiently large sphere covering the scene, which readily approximates radiance. We focus merely on the scattering pattern at this point, and hence disregard all wavelength-dependent effects,

rendering out an image with only one channel.

With the ten reflectance profiles from the database introduced in Chapter 3, we fit for each fur/hair sample a set of parameter values for the coaxial cylinder model. In our fitting procedure, the initial guess is manually devised based on our prior knowledge about each fur type and the scattering theory for fur fibers. We then leverage a trust-region-reflective algorithm as our non-linear optimization procedure for minimizing the pixel-to-pixel root-mean-square error between the synthetic and acquired reflectance profiles in natural log space.

$$\varepsilon_{\text{RMS}} = \sqrt{\frac{\sum_{\theta,\phi}\left[\log(f(\theta,\phi)) - \log(\hat{f}(\theta,\phi))\right]^2}{N}}, \tag{4.5}$$

where N is the number of pixels, $f(\theta,\phi)$ is a synthetic reflectance profile of coaxial cylinder model, and $\hat{f}(\theta,\phi)$ is an acquired reflectance profile in the fur database. The results from the fitting procedure for all ten samples, compared to the measurement data, are shown in the left two columns of Figure 4.3. We also directly plug the fit parameters into our practical shading procedure, introduced in Chapter 5, and generate synthetic reflectance profiles as shown in the rightmost column of Figure 4.3. Fit parameters for each fur sample, and the normalized root-mean-square (NRMS) errors for both the coaxial cylinder model and our practical shading approach, compared to the measurement data, are shown in Table 4.2. Formally, the normalized root-mean-square errors are

$$\varepsilon_{\text{NRMS}} = \frac{\varepsilon_{\text{RMS}}}{\max_{\theta,\phi}\log(\hat{f}(\theta,\phi)) - \min_{\theta,\phi}\log(\hat{f}(\theta,\phi))}. \tag{4.6}$$

The low normalized root-mean-square errors indicate that both our simulation and practical shading procedure captures decently the scattering behavior of a real fur fiber.

To exhibit the contributions of the explicit cuticle and medulla components to the
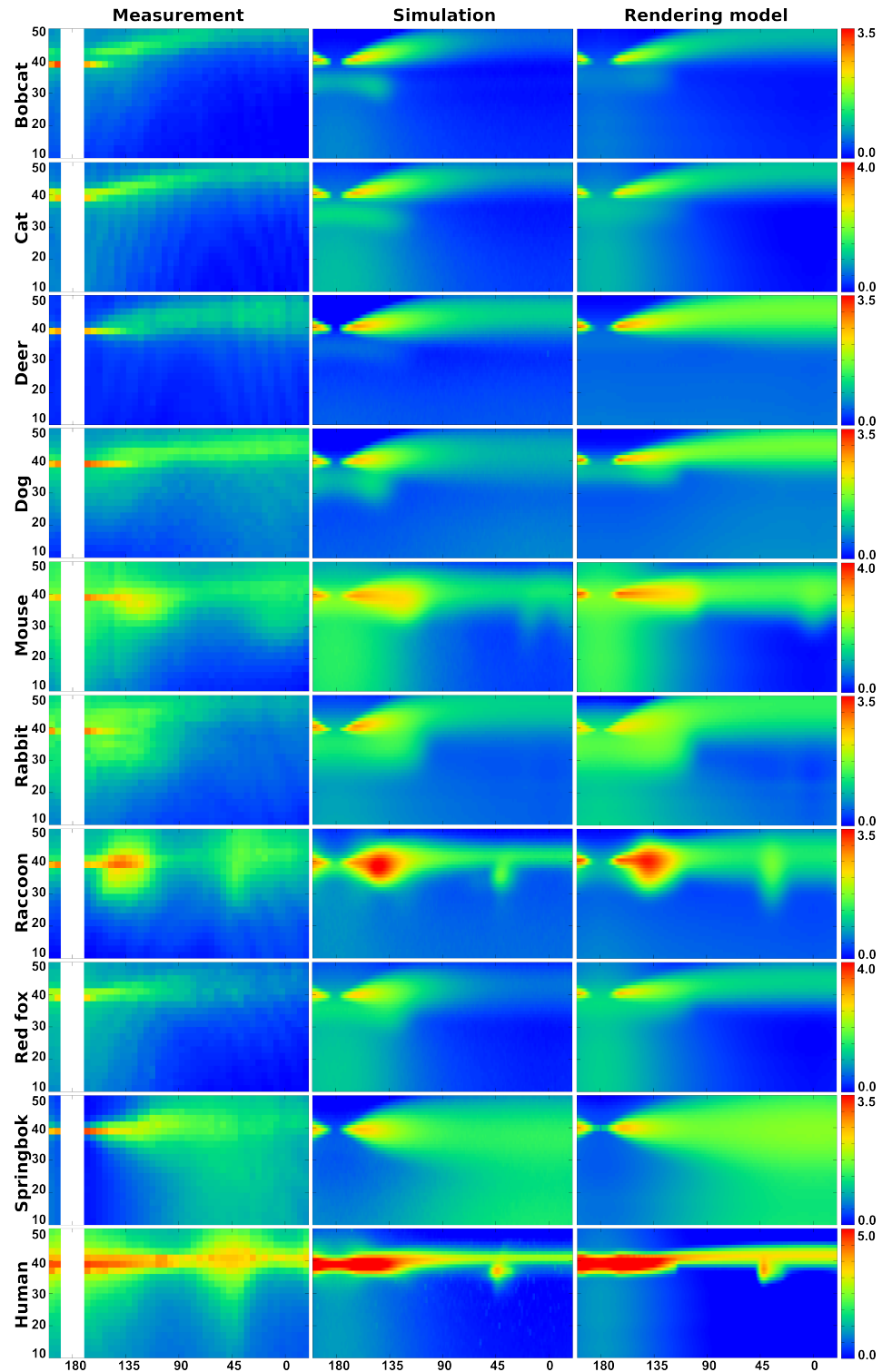
Figure 4.3: (Left) Two-dimensional reflectance profiles from our fur database. (Middle) Synthetic reflectance profiles of coaxial cylinder model under parameters we fit from each fur sample. (Right) Synthetic reflectance profiles generated using our practical shading procedure under the fit parameters.

Table 4.2: (Top) Optimized parameters fit from our measurement reflectance data using the coaxial cylinder model. (Bottom) Normalized root-mean-squared errors of the coaxial cylinder model and our practical shading approach (see Chapter 5) using the same parameters.

Parameter	Unit	Bobcat	Cat	Deer	Dog	Mouse	Rabbit	Raccoon	Red fox	Springbok	Human
κ	unitless	0.78	0.85	0.87	0.69	0.60	0.66	0.59	0.69	0.85	0.34
η_c	unitless	1.40	1.43	1.54	1.55	1.38	1.36	1.23	1.43	1.55	1.21
η_m	unitless	1.27	1.35	1.42	1.37	1.38	1.34	1.23	1.38	1.32	1.21
α	degree	4.44	3.97	2.93	2.47	1.05	4.41	1.20	2.25	0.03	0.87
β	degree	4.86	4.94	5.35	4.21	4.70	6.97	5.27	4.86	8.43	2.03
$\sigma_{c,a}$	diameter^{-1}	0.75	0.48	1.81	0.37	0.50	0.83	0.38	0.73	0.96	0.83
$\sigma_{m,s}$	diameter^{-1}	3.18	2.58	2.75	3.17	2.93	2.53	3.45	2.99	3.06	4.30
g	unitless	0.54	0.62	0.39	0.18	0.65	0.31	0.35	0.63	0.03	0.38
l	unitless	0.50	0.59	0.69	0.53	0.89	0.65	1.51	0.53	0.54	1.49
Simulation NRMSE		8.1%	6.7%	8.4%	9.1%	7.8%	9.4%	12.2%	5.9%	8.4%	15.4%
Rendering model NRMSE		7.2%	5.3%	7.9%	9.1%	8.5%	8.4%	10.1%	6.3%	7.0%	19.3%
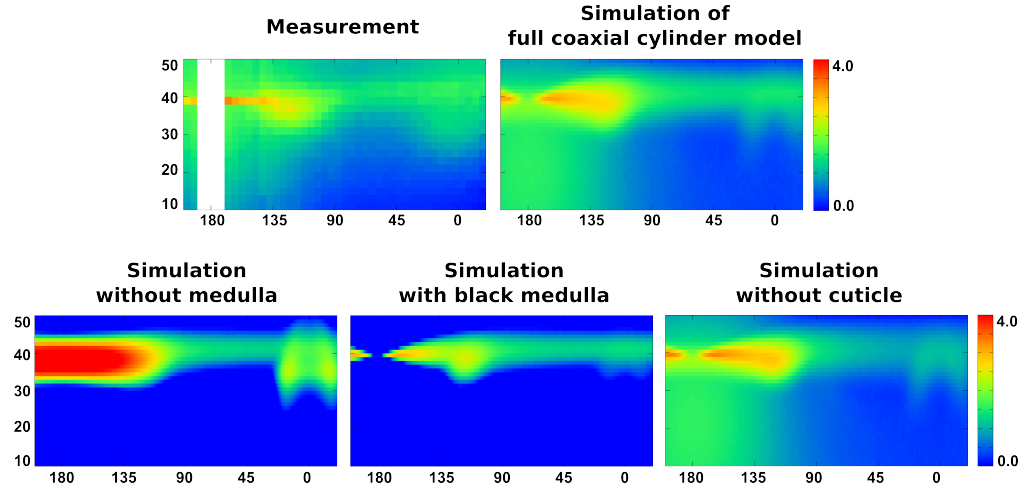
Figure 4.4: Comparison among synthetic two-dimensional reflectance profiles of the coaxial cylinder model, with and without the cuticle or the medulla component, and fit to the mouse fur fiber in our database.

appearance of our model, we compare the synthetic reflectance profiles with and without these components. The results are shown in Figure 4.4. It can be observed that, without an explicit cuticle, primary reflection in the synthetic reflectance profile becomes too dim to fit the measurement data in our database. Additionally, without an explicit medulla, the TT and TRT lobes can never get occluded, and thus cannot even qualitatively match the reflectance profiles in our database. Lastly, if we simply use a completely absorptive medulla, there appears to be no diffusive scattering at all in the synthetic profile. Overall, the explicit cuticle and medulla components contribute significantly to the synthetic BCSDF profile. Their contributions are consistent with what our scattering theory for animal fur fibers predicts.

Through qualitative and quantitative assessments in the BCSDF domain, we have solidly verified the scattering theory for fur fibers. We have shown that the coaxial cylinder model, which we propose based on the theory, is capable of producing all the scattering lobes observed on fur fibers from nine mammalian species and a human hair fiber. To this extent, the model provides a truthful representation of an animal fur fiber in the computational domain, which we can study, analyze and utilize as a primitive

for rendering photo-realistic fur. The establishments have enabled us to develop a more practical approach for shading animal fur fibers through deriving analytic and numerical approximations based on the coaxial cylinder model.

Chapter 5

Practical Shading Approach

The coaxial cylinder model enables us to run light transport simulation on an optically faithful representation of a fur fiber. However, as evaluating integrals over multiple volumetric scattering events is costly, the model remains impractical for rendering. In this section, we develop a practical rendering model, which can be plugged into global illumination renderers. We consider an enriched set of potential scattering paths in a fur fiber due to the presence of the medulla. All scattering paths we handle in our practical shading approach, besides the well-known TT and TRT paths as shown in 1.2, are illustrated in Figure 5.1.
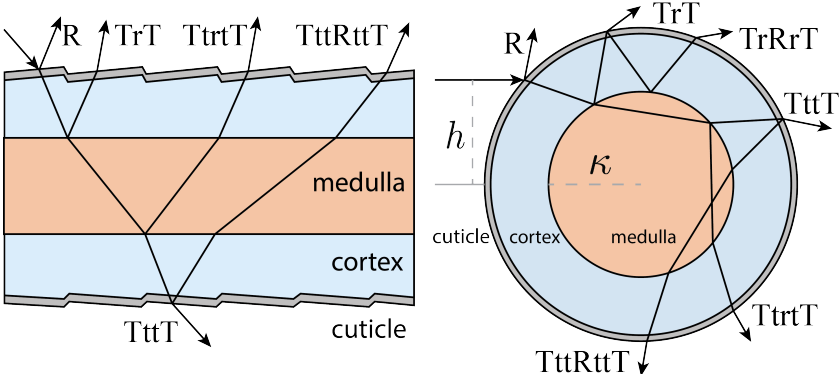
Figure 5.1: All scattering paths we consider in our practical shading approach, except the conventional TT and TRT paths.
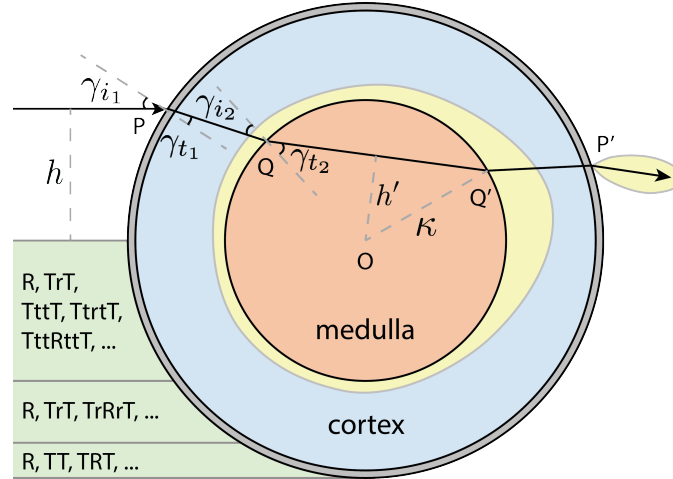
Figure 5.2: Illustration of evaluating the azimuthal scattering function for the $TttT$ scattering path.

5.1 Overview

Under the far-field approximation, most prior reflectance models for hair obtain a compact BCSDF for the fiber. To model the more sophisticated appearances of fur at a close distance, we find it essential to include near-field effects. Thus, we analyze the potential scattering paths for an incoming ray hitting the double cylinder, based on its incident position and direction.

We make this approach practical through a few key approximations. First, our near-field model incorporates factored approximation for rendering, similar to far-field hair models [MJC$^+$03, dFH$^+$11]. However, unlike those models, which consider a longitudinal and an azimuthal reflectance profile being generated collectively by all collimated incident rays over the width of the fiber, we consider an azimuthal and a longitudinal distribution being generated by each ray we trace through the fiber. This approach is equivalent to having varying BCSDFs over h in Figure 5.1, which makes our model compatible with the far-field BCSDF framework, yet enables near-field effects. In [ZW07], the approach we use is classified as a near-field scattering model with constant incident illumination. Hence, we can leverage previous work, keeping the R, TT and

TRT terms identical, but adding lobes for *TrT*, *TttT*, *TtrtT*, *TrRrT* and *TttRttT* paths, indicated in Figures 5.1 and 5.2. Note that our framework can also handle general higher-order scatterings, but in our experiments, the contributions from those paths was insignificant.

It remains to find the forms of azimuthal and longitudinal scattering functions for each lobe. Conceptually, given the incident position and direction of a ray that enters the fiber, we ray-trace its chief specular ray [dFH+11, ZYWK08] on the 2D azimuthal cross section of the fiber. We consider the direction at which the chief specular ray leaves the fiber as the center of a reflectance lobe, and accumulate the attenuation factors, and the azimuthal and the longitudinal roughnesses along the specular path, in the form of a Gaussian outgoing lobe. This is shown for the *TttT* path $PQQ'P$ in the azimuthal section in Figure 5.2. In practice, rays are traced using closed-form analytic formulae. Longitudinal distributions are further simplified to conform to previous work, reducing to Gaussians with offsets/width for effective cuticle tilt/roughness. Finally, for those paths that enter the medulla, and are *scattered* by it, we must also include a scattered lobe (see broad yellow lobe at Q' in Figure 5.2). We precompute medulla scattering separately for 2D azimuthal/longitudinal profiles (Figure 5.3), based on [DLR+09], reducing scattering to a table lookup.

Formally, the near-field scattering distribution for each ray is,

$$S(\theta_i, \theta_r, \phi_i, \phi_r, h) = \frac{\sum_p M_p^u(\theta_i, \theta_r) N_p^u(h, \phi)}{\cos^2 \theta_i} + M^s(\theta_i, \theta_r, \phi) \frac{\sum_p N_p^s(h, \phi)}{\cos^2 \theta_i}, \qquad (5.1)$$

where

$$p \in \{R, TT, TRT, TrT, TttT, TtrtT, TrRrT, TttRttT\},$$

and M_p and N_p are respectively longitudinal and azimuthal scattering profiles that depend on the fur parameters in Table 4.1. Note the *h* parameter (Figures 5.1, 5.2) for near-field

scattering. The superscripts *s* and *u* stand respectively for paths *scattered* by the medulla, and *unscattered*. (We will see that a single longitudinal M^s is adequate for all scattered paths *p*). The paths *p* include *R*, *TT* and *TRT* from previous hair models, as well as new terms specific to fur. Note that only unscattered lobes will be present for *R*, *TT*, *TRT*, *TrT*, *TrRrT* paths that never transmit into the medulla, while *TttT*, *TtrtT* and *TttRttT* will have both scattered and unscattered lobes. Finally, we choose to replace the $1/\cos^2 \theta_d$ term with $1/\cos^2 \theta_i$ per [HR12] to mitigate the energy conservation issues at grazing angles analyzed by [dFH$^+$11].

Simple lobes. Consider rays that do not enter the medulla at all.

$$p \in \{R, TT, TRT, TrT, TrRrT\}.$$

In this case, there is no scattering from the medulla, and we can drop the superscripts. The azimuthal profile is simply

$$N_p(h, \phi) = A_p(h) \cdot D_p(h, \phi), \tag{5.2}$$

where A_p is the attenuation along path *p*, and D_p is the azimuthal distribution of scattered energy, a Gaussian with width determined by considering the roughness from all the surfaces the ray has interacted with. For the longitudinal profile of a ray, we follow [MJC$^+$03, dFH$^+$11] and approximate it with a Gaussian distribution,

$$M_p(\theta_i, \theta_r) = G(\theta_r; -\theta_i + \alpha_p, \beta_p), \tag{5.3}$$

where α_p is the accumulative angular tilt of the chief specular ray on path *p* due to interaction with the cuticle scales, and β_p is the roughness for path *p*, which is empirically

given by accumulating cuticle roughness. These expressions reduce to previous work for the lobes R, TT, TRT from the hair model. We now proceed to develop general formulae for paths that interact with the medulla.

5.2 Unscattered Lobes

We first discuss lobes that are not scattered by the medulla, giving expressions for M_p^u and N_p^u. Consider the azimuthal profile in Figure 5.2. Conceptually, we simply ray-trace the chief specular ray incident at P in the 2D azimuthal cross-section, accumulating attenuation and surface roughness along the path to give the intensity and width of the outoging Gaussian lobe centered at P'. In practice, ray-tracing can be replaced with simple analytic formulae.

An interesting observation is that certain types of paths only happen in specific zones over the offset h (see Figure 5.2). For example, depending on the size of the medulla, the traditional hair model paths T, TT and TRT are only possible for large h, and must enter the medulla otherwise. In practice, we solve geometrically for the boundaries of these zones, corresponding to $\gamma_{i_2} = 90°$ and $\gamma_{t_2} = 90°$, and only consider the relevant paths within each zone.

Azimuthal scattering profile. The azimuthal profile is given by equation 5.2, but additional handling is required for chief specular rays that hit and enter the medulla.

$$p \in \{TttT, TtrtT, TttRttT\}.$$

We split the contribution into two terms: the multiple scattered light for which we compute M^s and N^s in the next section based on precomputed medulla scattering; and the unscattered light considered here, which is simply attenuated as it passes through the

medulla. For instance, in a *TttT* path as shown in Figure 5.2,

$$N_p^u(h, \phi) = A_{Tt}(h) \cdot A_{tt}(h) \cdot A_{tT}(h) \cdot D_p^u(h, \phi). \tag{5.4}$$

Here, $A_{tt}(h)$ is the attenuation factor for a chief specular ray transmitting through the medulla (QQ' in Figure 5.2).

With this background, a simple expression can be written for general higher-order paths, which can also be used for our *TtrtT* and *TttRttT* lobes. If we regard p as a string of length n, while p_i ($i = 1 \ldots n$) represents each vertex in p, we can write

$$A_p(h) = \prod_{i=1}^{n} F(p_i) \cdot \prod_{i=2}^{n} \exp(-\sigma_t(p_{i-1}p_i) \cdot |p_{i-1}p_i|) \tag{5.5}$$

where F is the (extended) Fresnel term, $|p_{i-1}p_i|$ is the length of segment $p_{i-1}p_i$, and $\sigma_t(p_{i-1}p_i)$ equals either $\sigma_{c,a}$ of the cortex or $\sigma_{m,s}$ of the medulla, as the segment's extinction coefficient.

Similarly, at every intersection, the direction of p alters by angle $\Gamma(p_i)$. Thus, the outgoing azimuth could be computed by accumulating these deviation angles as $\Phi_p(h) = \pi + \sum_{i=1}^{n} \Gamma(p_i)$, where π accounts for the inversion of the incoming direction. For the distribution term D, similar to [dFH+11, ZYWK08], we accumulate the roughness i.e., β^2 at each intersection p_i along the path p. Since the outgoing distribution is a Gaussian lobe G centered at $\Phi_p(h)$, we can derive an analytic form,

$$D_p^u(h) = G\left(\Phi_p(h), \sqrt{\sum_{i=1}^{n} \beta^2(p_i)}\right) \tag{5.6}$$

where $\beta(p_i) = 0$ if the intersection p_i is not on the cuticle. Explicitly, the width is given by the number of upper-case (cortex) letters, and is β for $p \in \{R\}$, $\sqrt{2}\beta$ for $p \in \{TT, TrT, TttT, TtrtT\}$, and $\sqrt{3}\beta$ for $p \in \{TRT, TrRrT, TttRttT\}$.

Longitudinal scattering profile. The unscattered longitudinal profile is given by equation 5.3. All that remains is to determine the center α_p and width β_p of the unscattered lobes. We follow previous work for R and TT lobes, setting $(\alpha_R, \beta_R) = (\alpha, \beta)$ for R, corresponding to the cuticle tilt and roughness, while $(\alpha_{TT}, \beta_{TT}) = (-\alpha/2, -\beta/2)$. For other lobes, we approximate

$$\alpha_p = \alpha_{TT} - n_R \alpha$$

$$\beta_p = \beta_{TT} + n_R \beta + (n \bmod 2)(\beta/2), \tag{5.7}$$

where n is the length of p, and n_R is the number of Rs appearing in p. The general idea is that, every reflection on the cuticle decreases its tilt angle and increases roughness. The final $\beta/2$ compensates for lobes exiting backwards, since they are usually wider than forward lobes [dMH14]. Thus, $\alpha_p = \alpha$ for $p \in R$, $\alpha_p = -\alpha/2$ for $p \in \{TT, TrT, TttT, TtrtT\}$ and $\alpha_p = -3\alpha/2$ for $p \in \{TRT, TrRrT, TttRttT\}$. Similarly, $\beta_p = \beta/2$ for $p \in \{TT, TttT\}$, $\beta_p = \beta$ for $p \in \{R, TrT, TtrtT\}$ and $\beta_p = 2\beta$ for $p \in \{TRT, TrRrT, TttRttT\}$. Note that, to our knowledge, longitudinal lobes' parameters were *empirically given* in most previous work; equation 5.7 provides a reasonable approximation to extend prior work to general paths that may enter the medulla.

5.3 Scattered Lobes

When the path $p \in \{TttT, TtrtT, TttRttT\}$ goes through the inner cylinder, scattering events happen, and this medulla scattering needs to be taken into account (the broad yellow lobe from Q' in Figure 5.2). We rely on precomputation, and make a number of significant approximations to the full volumetric multiple scattering computation, to

---

[1]In the precomputation, we assume all sub-paths are entering the medulla horizontally, since the azimuthal section is rotationally-invariant.
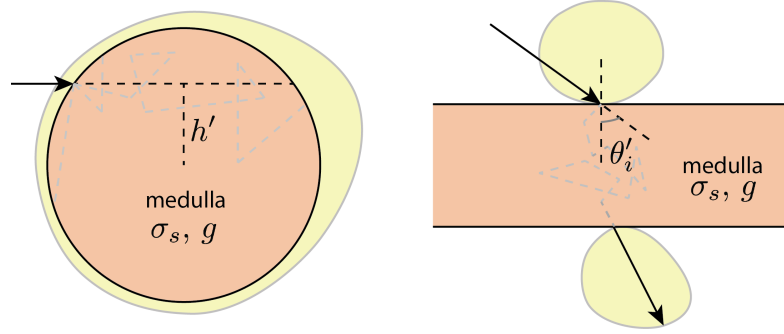
Figure 5.3: Precomputing medulla scattering. We enumerate $\sigma_{m,s}$ and g, and vary azimuthal offset h' and longitudinal incident angle θ'_i respectively.[1] We store the yellow-marked scattered lobe in every outgoing azimuth ϕ' and longitudinal outgoing angle θ'_r.

enable a practical rendering model.

Precomputation of medulla scattering. Our precomputation approach is similar in spirit to the empirical BSSRDF model by [DLR+09]. However, since we use factored lobes, we precompute scattering profiles by 2D volumetric path-tracing separately for azimuthal and longitudinal components, for all possible combinations of scattering parameters, as illustrated in Figure 5.3. Here, we don't consider surface effects (reflection, refraction, Fresnel, etc) for the medulla; instead we compute these effects in the evaluation steps. In effect, we are precomputing 4D tables $C^N(\phi'; h', \sigma_{m,s}, g)$ azimuthally and $C^M(\theta'_r; \theta'_i, \sigma_{m,s}, g)$ longitudinally (1D profiles for 3D sets of parameters). We use primes to distinguish notation from the main parameters. Our precomputation is entirely scene-independent, and only needs to be done once. After compression, these tables takes up only about 20 megabytes. Details are discussed in Appendix A.

Azimuthal scattering profile. The scattering lobe is usually large and diffusive, and therefore not significantly affected by the smaller effects of surface roughness. We also ignore refraction by the cortex-air interface, and assume that the light leaving the medulla is attenuated by a constant factor corresponding to the thickness of the cortex. Moreover,

we assume that the precomputed scattered lobe from the medulla doesn't change its shape after transmitting outside. Finally, we assume that there is only one scattered lobe that is not further reflected by the cortex; Appendix A discusses a first step towards relaxing this assumption.

In analogy to equation 5.4, the azimuthal scattering profile from a $TttT$ path is,

$$N_p^s(h, \phi) = A_{Tt}(h) \cdot A_{tT}'(h) \cdot D_p^s(h, \phi). \tag{5.8}$$

Note that the distribution D^s is not normalized, and accounts for the reduction in energy $1 - A_{tt}(h)$ due to the unscattered lobe already considered. The final attenuation A_{tT}' is now approximated simply as $\exp[-\sigma_{c,a} \cdot (1 - \kappa)]$, corresponding to the thickness of the cortex. We simply need to add one more attenuation term for $TtrtT$,

$$N_p^s(h, \phi) = A_{Tt}(h) \cdot A_{tr}(h) \cdot A_{tT}'(h) \cdot D_p^s(h, \phi). \tag{5.9}$$

Note that the scattered lobe arises only on the final rt segment; any scattering in the earlier segment will be considered as part of $TttT$. A similar expression can be used for the $TttRttT$ lobe. More generally, the attenuation of a scattered lobe consists of two parts. First, the energy reaches into the medulla. Second, the scattered energy is further absorbed, transmitting through the cortex.

The distribution term D for a scattered lobe is simply a query into the precomputed azimuthal scattering profile $C^N(\phi'; h', \sigma_{m,s}, g)$. Since we precompute the medulla as a unit circle, h' and $\sigma_{m,s}$ need to be normalized by radius κ, leading to

$$D_p^s(h, \phi) = C^N(\phi - \Phi_p(h); h'/\kappa, \sigma_{m,s}/\kappa, g), \tag{5.10}$$

where Φ_p is the angle at which the ray enters the medulla.
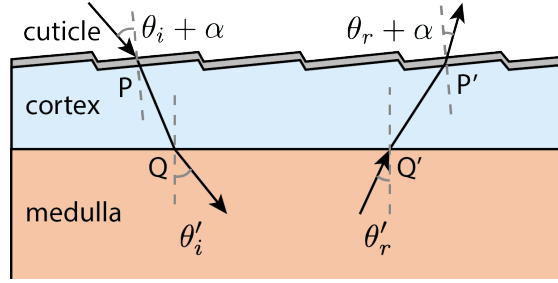
Figure 5.4: Illustration for computing longitudinal scattering function for the scattered components, M^s. Refractions are considered here at P, Q, P' and Q'.

Longitudinal scattering profile. The longitudinal scattered lobe M^s is p-independent, because every type of path p has the same θ_i and θ_r. However, it is ϕ-dependent. As Figure 5.3 illustrates, the longitudinal profiles we precompute are for $\phi = 0$ (the upper lobe) and $\phi = \pm 180°$ (the lower lobe). We compute M^s at both azimuths, and linearly interpolate the results for any ϕ. Thus, for simplicity we omit ϕ in the following, and take $\phi = 0$ for illustration.

We query the precomputed longitudinal distribution for the medulla C^M, considering refractions through the cuticle and the cortex. As Figure 5.4 shows, θ'_i and θ'_r could be solved geometrically. Similar to the azimuthal case, we query the precomputed distribution at θ'_r,

$$M^s(\theta_i, \theta_r) = \mu \cdot F_t \cdot C^M(\theta'_r; \theta'_i, \sigma_{m,s}/\kappa, g), \tag{5.11}$$

where $F_t = (1 - F(\theta_r + \alpha, l)) \cdot (1 - F(\theta'_r))$ is the product of (extended) Fresnel transmittance, and μ is the normalization factor which is described in detail in Appendix A.

5.4 Implementation and Validation

Importance sampling. Our importance sampling scheme is similar to [dMH13], where we first perform a lobe selection, then sample this lobe azimuthally and longitudinally.

Here, we treat all scattered lobes together. If an unscattered lobe p is chosen, we sample a Gaussian around its azimuthal outgoing center $\Phi_p(h)$ and its longitudinal outgoing center $-\theta_i + \alpha_p$. This leads to a near-perfect importance sampling scheme. If the (summed up) scattered lobe is chosen, we perform a cosine-weighted sampling longitudinally and a uniform sampling azimuthally, taking advantage of the fact that the scattered lobe is smooth. For multiple importance sampling, which queries the PDF at a given outgoing direction, we first perform a lobe selection similarly, then compute the corresponding PDF value at the outgoing direction, depending on whether the scattered or unscattered lobe is selected.

Non-separable lobes. In [dMH14], the non-separable lobes representation was introduced to accurately capture light scattering through a hair fiber. In this representation, the center and width of longitudinal lobes further depends on the relative azimuth ϕ. Indeed, there are quality improvements in rendering results from the original paper. However, we find that the main difference is the shape of the R lobe, which is the only one that spans a large range over azimuthal angles. Thus, when applied to our double cylinder model, we simply represent our R lobe as non-separable, and leave other lobes using the traditional representations.

Validation. We compare 2D profiles generated using our rendering model with measured data and simulations in Figure 4.3. Our rendering model closely matches the measured reflectance profiles, and has comparable error (Table 4.2) to a full simulation, in some cases even being closer to the measurements. This is not surprising, since the physical double cylinder model is exactly the same. Minor discrepancies are due to approximations, such as factoring longitudinal and azimuthal scattering profiles, empirical longitudinal lobe centers and widths, and medulla scattering approximations.

Chapter 6

Results and Conclusion

6.1 Renderings

In this section, we show results generated using our rendering model, and visual comparisons to previous methods. All results use our rendering model as a shader within Mitsuba [Jak10], run on an Intel 6-core 3.6 GHz i7 4960X CPU, hyperthreaded to 12 threads. Statistics of each scene such as number of strands, number of samples and timings are listed in Table 6.1. The times are total wall clock running time, including global illumination; the cost of evaluating our model is comparable to that of the Marschner model, which produces almost identical timings. For all the scenes, all parameters are

Table 6.1: Statistics of all of our renderings. We represent fur fibers using line segments for each fur fiber. # Strands is the number of fur fibers, and # Segments is the number of segments along each fur fiber.

	Wolf	Chipmunk	Cat	Fur pelt
# Strands	1.6 M	503 K	729 K	12.5 K
# Segments	8	8	10	5
Area light		✓		✓
Environment light	✓	✓	✓	
# Samples per pixel	1600	1600	2500	1024
Time	60.8 min.	23.6 min.	56.2 min.	12.4 min.

(a) $\sigma_{m,s} = 0.75$ (b) $\sigma_{m,s} = 1.5$ (c) $\sigma_{m,s} = 3.0$ (d) $\sigma_{m,s} = 6.0$

Figure 6.1: Renderings of the Cat scene under environment lighting using our practical shading approach with various medulla scattering coefficients ($\sigma_{m,s}$).

(a) $\kappa = 0.25$ (b) $\kappa = 0.5$ (c) $\kappa = 0.75$ (d) $\kappa = 0.99$

Figure 6.2: Renderings of the Cat scene under environment lighting using our rendering model with various medulla size (κ).

directly derived from our database in Table 4.2, except for the absorption term $\sigma_{c,a}$ which accounts for different colors.[1] We also account for the fact that the medulla does not absorb light, by multiplying $\sigma_{c,a}$ by the medullary index κ. For wolf and chipmunk, since we don't have corresponding fur samples, we refer to parameters for dog and mouse from our database instead.

In comparisons, we consider [dFH+11] as a correct implementation of the Marschner model, so that the dark appearance generated is due to specularity of the model itself, rather than energy conservation issues. For the Marschner model, we also use its own set of optimized fitting parameters to our fur database, rather than ad-hoc settings from industry such as enlarging azimuthal roughness. For the Kajiya-Kay model, we enable global illumination by normalizing equation 1.2, since the model itself is not energy conserving.

Wolf. Figure 6.3 shows our rendering result for a Wolf model with a side-by-side comparison with the Marschner model. The environment lighting is manually blurred prior to rendering. Insets are provided to compare with the Marschner and Kajiya-Kay models. All the renderings are path traced (for global illumination between fibers and the environment) using 1600 samples per pixel (spp) at a resolution of 1920×1080. Our double cylinder model produces a diffusive and saturated appearance, while the Marschner model is highly specular and dark. Note that, our method actually produces brighter highlights with the layered cuticle model than Marschner, but these are less *visually* obvious due to low local contrast. The Kajiya-Kay model produces a hard and solid appearance even with global illumination. Intuitively, compared to our model, it is visually similar to a BRDF vs BSSRDF (BCSDF) comparison.

---

[1] For comparisons, we use colored textures to assign $\sigma_{c,a}$ in the Marschner model for each fiber rooted at texture coordinate (u,v) as $\sigma_{c,a} = -\log(T(u,v))/4$, where $T(u,v) \in [0,1]$ is the texture color at (u,v), considering each color channel.

Figure 6.3: Renderings of the Wolf scene under environment lighting using our practical shading approach with parameters from our database of mammalian fur samples, and energy conserving Marschner model.

Cat.   In Figures 6.1 and 6.2, we render a close-up view of a cat head with depth of field effects under environment lighting, showing details of each fur fiber. We use our optimized fit parameters for cat fur in our database. All renderings use a sampling rate of 2500 spp with resolution 1024×1024. We can see that our rendering produces both a blurred area (top left of the eye) and distinct appearance (around the whisker) due to different arrangements and orientations.

We also show how an artist can manually vary key parameters of the model to get a range of appearances. Figures 6.1 and 6.2 show renderings with varying scattering coefficients $\sigma_{m,s}$, as well as medulla size κ. We observe that, artistically, $\sigma_{m,s}$ closely controls color saturation, and κ determines the "specularity", or the extent of similarity between hair and fur.

Chipmunk.   Figure 6.4 is rendered with a sharp and strong area light, and a relatively dim environment light. The skin of the chipmunk is dark colored. The Marschner model again produces unrealistically specular and dark appearance, since the light easily penetrates the fibers and hits the skin. However, primary (uncolored) and secondary (colored) highlights are still visible in the Marschner model. Both models are rendered using 1600 spp at resolution 1920×1080.

Fur pelt.   Figure 6.5 contains a pelt of fur placed on a checker board rendered using 1024 spp with resolution 1024×1024. A large area light illuminates the pelt from the top-left. Our model gives a realistic diffusive and saturated appearance, while the Kajiya-Kay model looks hard and solid. The Marschner model produces classic primary and secondary highlights, but leaves other regions black. By blending a diffuse lobe into the Marschner model as proposed by [ZRL+09] (a solution that is widely adopted by the industry), one can generate a diffusive appearance. However, the blending technique lowers the intensity of the original lobes in the Marschner model, especially for the

Figure 6.4: Renderings of the Chipmunk scene using our practical shading approach and Marschner model illuminated with a strong area light and a dim environment light.
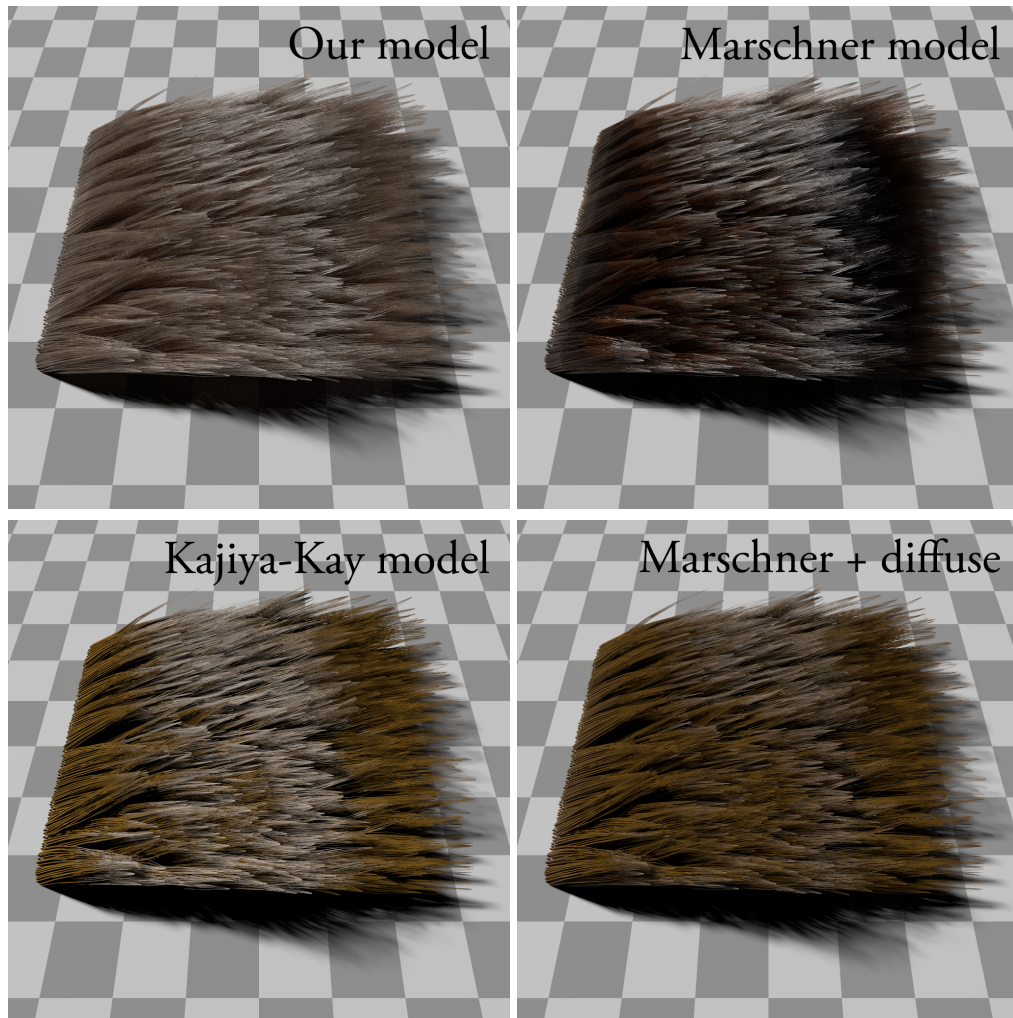
Figure 6.5: Renderings of the Fur pelt scene under area lighting. (Top left.) Our practical shading approach. (Top right.) Marschner model. (Bottom left.) Kajiya-Kay model. (Bottom right.) Marschner model blended with diffuse lobe.

reflected lobe R, which leads to a flat appearance. Furthermore, this approach is empirical and the existence of the diffuse lobe cannot be explained physically.

6.2   Retrospect

The coaxial cylinder model produces highly accurate reflectance fields of animal fur fibers that match well the two-dimensional far-field reflectance data from real-world measurements on multiple fur samples. By analyzing the influence of the subsurface structures in a fur fiber to its macroscopic appearance, we are able to uncover scattering mechanisms behind many reflectance phenomena, especially the rough appearance of fur, that have been long known but yet understood.

In Figure 6.6 and 6.7, we compare the synthetic profiles of the coaxial cylinder model to that of the Kajiya-Kay model, the Marschner model and the Marschner model with a diffuse lobe, as suggested by [ZRL$^+$09]. Since the Marschner model is purely specular, it fails to fit well to most measurement data, except in the case of a human hair, where specular reflectance dominates. Even when a diffuse lobe is blended into it, it still cannot match the measurement reflectance data. This is because the blended-in diffuse lobe is always symmetric longitudinally at $\theta = 0°$ and does not distinguish forward and backward scattering effects. As for the Kajiya-Kay model, since the reflectance profile it generates is azimuthally independent and is merely composed of a diffuse lobe and a specular cone at a fixed angle, its controllability is extremely limited, and fits poorly to all the measurement data.

Scientifically, it would be interesting to further explore possible scattering mechanisms in a fur fiber and fix the cases where the current coaxial cylinder model fail. For instance, it can be observed in Figure 4.3 that the sharp R peak and the long tail which decorates all the specular R, TT and TRT lobes still cannot be modeled accurately using
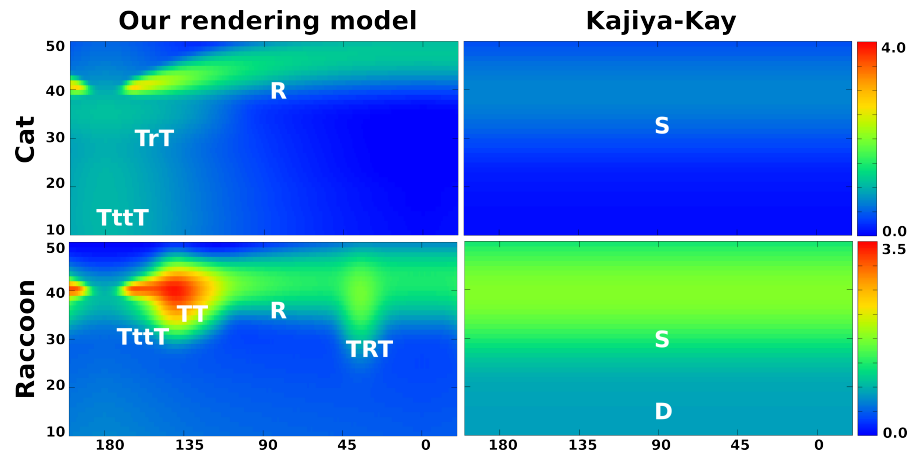
Figure 6.6: Comparison between synthetic reflectance profiles generated using our practical shading approach and the Kajiya-Kay model. S indicates the specular lobe and D indicates the diffuse lobe.
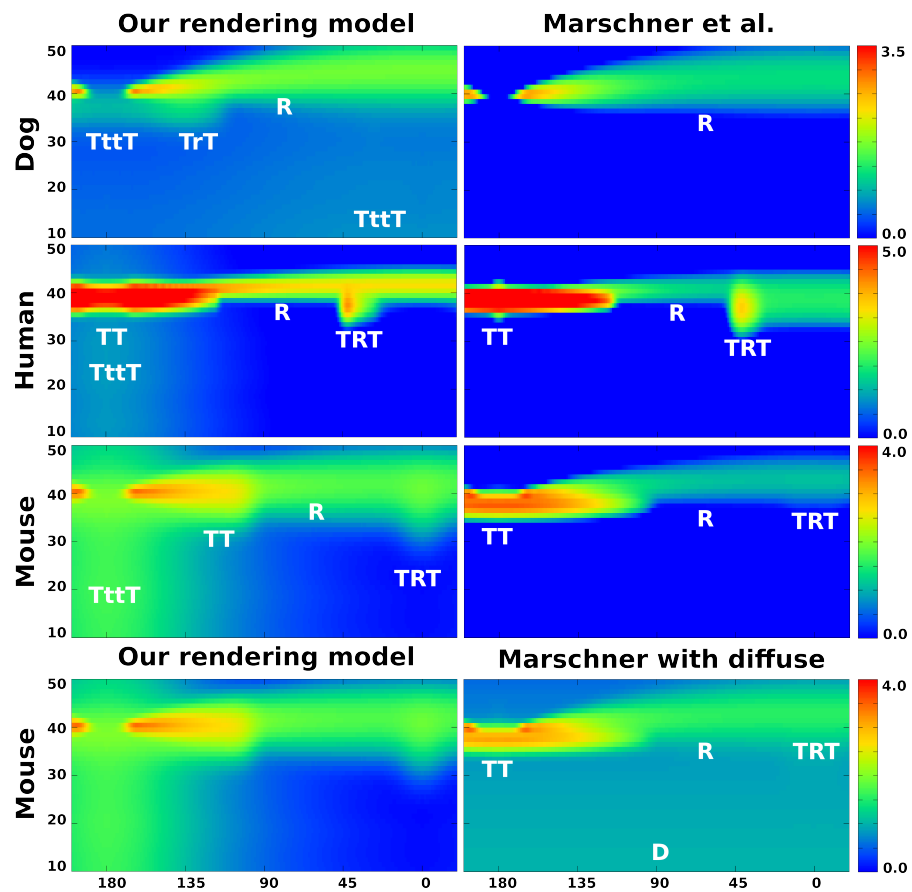
Figure 6.7: Comparison between synthetic reflectance profiles generated using our practical shading approach and the Marschner model, with or without an additional diffuse lobe, denoted D.

Figure 6.8: Rainbow glints captured on a raccoon fur pelt under direct sunlight.

either prior reflectance models or our coaxial cylinder model. An initial attempt has been made to address these effects by considering internal reflections between cuticle scales and the endocuticle roughness. The derivation is included in the appendix B of this thesis for completeness. Other interesting effects observed on fur fibers include rainbow glints that are seen even on black fur fibers under sunlight (Figure 6.8), which we believe to arise from thin-film interference over the cuticle, as elaborated in Chapter 3.

However, while we achieve dramatic improvements in fitting quality over re-flectance profiles using the coaxial cylinder model, the improvements in photo-realism for our renderings are less dramatic. Interestingly, the Kajiya-Kay model, which fails to produce even matchable reflectance profiles to the measurement data, can simulate acceptable photo-realism, and the Marschner model with a diffuse lobe, though not physically-based and suffers the energy redistribution issue we mention in the previous section, actually performs well in terms of rendering quality. For more insights, it may be worthwhile to study light scattering from fur and hair fibers under the perceptual space of human vision.

6.3   Conclusion and Future Work

We present a physically-based fur reflectance model to accurately capture the appearance of animal fur fibers. Our model is near-field based, treating fur fibers as double cylinders, taking into account the existence of scattering medullas inside. We also derive a fast evaluation algorithm for rendering, built upon precomputed empirical medulla scattering profiles. We demonstrate that our rendering model fits the measured data well, with errors comparable to a full volumetric simulation. We also introduce the first database in computer graphics of reflectance measurements on a number of animal fur fibers, including both raw 2D scattering profiles and fit parameters. We show that our model is capable of generating a variety of realistic animal fur appearances, with more realistic results than previous methods.

In the future, we would like to explore possibilities to make our model completely analytic without precomputation. An extension to handle more features such as irregular fiber sections, complicated cuticle scale arrangements and discontinuous medullas would also be interesting. Industry may benefit if a re-interpretation from an artistic viewpoint is derived. Additionally, the introduction of the medulla and the cuticle increases the complexity of the reflectance model significantly. Therefore, it may be beneficial to look into potential redundancies in the high-dimensional parameter space and simplify the model. It may also be worthwhile to develop an algorithm for interactive and intuitive fur/hair materials editing. Finally, a fast and accurate way to approximate multiple scattering using our reflectance model would contribute greatly in real-time fur rendering applications.

Appendix A

Practical Shading Approach: Details

Precomputation and compression.   We enumerate scattering coefficient $\sigma_{m,s} \in [0, 20]$ and anisotropy $g \in [0.0, 0.8]$, and we vary an additional parameter specifying different incoming directions. For azimuthal profiles, it is the offset $h' \in [-1, 1]$ assuming all sub-paths are entering the medulla horizontally (Figure 5.3). For longitudinal profiles, it is the incident angle $\theta_i' \in [-\pi/2, \pi/2]$. We discretize the range of g into 16 steps, while for all other parameters, we use 64 steps.

We separately simulate the medulla's azimuthal and longitudinal scattering profiles using volumetric path tracing in 2D, assuming that the incident path carries unit energy. We trace a smooth unit circle azimuthally and a double slab with distance 2 in between longitudinally. For all scattering events, we use the planar Henyey-Greenstein phase function [Dav06],

$$\rho(\theta; g) = \left(\frac{1}{2\pi} \right) \frac{1 - g^2}{1 + g^2 - 2g\cos\theta},\tag{A.1}$$

to consider anisotropicity, where θ is the angle each scattering event deviates from its earlier path.

Each precomputed outgoing profile is stored using 720 bins covering every

direction, recording the exiting energy. For longitudinal scattering, we further normalize the upper and lower lobes respectively, making both of them probability density functions. Then we accumulate their cumulative density functions for convenience in the next steps.

Refining the azimuthal scattered lobes. Due to Fresnel effects, the scattered lobe could be reflected back by the surface of the medulla and the cuticle, thus undergoing further scattering, making it even smoother. We approximate this proportion as $\lambda = 1 - (1 - F(\pi/2))(1 - F(\pi/2, l))$, which is simply the leftover energy after perpendicularly transmitting through two interfaces, ignoring multiple internal reflections. So the azimuthal scattered lobes can be extended to

$$N_p^s(h, \phi) = A_p^s(h) \cdot \left[D_p^s(h, \phi) \cdot (1 - \lambda) + I_j^s \cdot \lambda \right], \tag{A.2}$$

where $I_j^s = [1 - \exp(-\sigma_{m,s} \cdot |p_j p_{j+1}|]/2\pi$ is uniform distribution of the scattered energy, under the assumption that the reflected back scattered lobe will become isotropic after more scattering events. j is the location of the vertex where the path enters the medulla and scatters, and A^s is the effective attenuation for the scattered lobe.

Normalizing the longitudinal scattered lobe. Since our final longitudinal scattered lobe M^s is normalized, we have $\int M^s \, d\theta_r = 1$. According to Equation 5.11, we have $\int F_t \cdot C^M \, d\theta_r = 1/\mu$. Then, approximately we have $\int F_t \, d\theta_r \cdot \int C^M \, d\theta_r = 1/\mu$. Denoting these two separated integrals as U and V, we found that U can be numerically calculated when a certain species of fur is loaded in, which introduces no overhead when rendering on the fly. For V, we first convert the integration domain into θ_r', using $\frac{d\theta_r'}{d\theta_r} \approx \frac{\cos \theta_r}{\eta_c \cos \theta_r'}$ by differentiating the formula for Snell's law at P' and Q'. Then we know the range of θ_r' that C^M should be integrated in. Since the precomputed C^M is a normalized PDF, the integration is a query on its CDF, which is simply accumulated in the precomputation

step. Thus, we have $\mu = (UV)^{-1}$ as our normalization factor.

Appendix B

A More Accurate Cuticle Model

We start out formulating an analytic model for cuticle by approximating it with a single interface. This approximation is valid since we consider that the cuticle is a very thin layer within the volume of a fur fiber. Since the cuticle scales are known to be composed of dielectric materials with no absorption, we can naturally assume the approximating interface to be a rough dielectric one without any compatibility issue. Therefore, the problems remain is to resolve physically the effective reflectance and the effective half-vector distribution for this approximating interface.

We look into literature in physics to resolve the collective reflectance of cuticle scales, where the optical properties of a pile of dielectric plates have been extensively studied, formalized as waves propagating in stratified media. While there is recent research effort in computing the overall reflectance and transmittance of a pile of *rough* dielectric plates, these methods involve wave optics, rendering them inherently incompatible to a standard ray tracer. They are also overly complicated for our purpose of forming a simple shading model for a fur fiber. Fortunately, for a pile of *smooth* dielectric plates, a closed-form solution purely in the regime of geometric optics has been derived as early as in 1860 in [Sto60]. Formally, the collective reflectance for a pile of *l* separated,

non-absorbing plates is found to be

$$F(\theta_i; l) = \frac{m \cdot F(\theta_i; 1)}{1 + (m - 1) \cdot F(\theta_i; l)}. \tag{B.1}$$

where $F(\theta_i; 1)$ is the reflectance for a single plate. The collective transmittance is thus

$$T(\theta_i; l) = \frac{1 - F(\theta_i; 1)}{1 + (m - 1) \cdot F(\theta_i; 1)}. \tag{B.2}$$

The value of $F(\theta_i; 1)$ can be computed directly from a geometric series with its common ratio dependent on the s-polarized Fresnel reflectance ($F_s(\theta_i)$) and the p-polarized Fresnel reflectance ($F_p(\theta_i)$). For unpolarized light,

$$F(\theta_i; 1) = \frac{1}{2} \left\{ F_s(\theta_i) + \frac{[1 - F_s(\theta_i)]^2 F_s(\theta_i)}{1 - F_s(\theta_i)^2} \right\} + \frac{1}{2} \left\{ F_p(\theta_i) + \frac{[1 - F_p(\theta_i)]^2 F_p(\theta_i)}{1 - F_p(\theta_i)^2} \right\}. \tag{B.3}$$

Although we consider this formulation sufficient for the purpose of forming a practical and controllable shading model for cuticle, we must state that it is not completely accurate when applying to a rough interface. This is because, by incorporating the closed-form solution to our model, we are actually perturbing *correlatively* all the half-vector distributions that are involved within one scattering event on the approximating interface. Hence, a more accurate treatment is required for higher precision.

We now turn to resolving the collective microfacet distribution. We first consider only a single layer of exocuticle from the cuticle scales. It is natural to assume Beckmann half-vector distributions on both the inner and the outer interfaces. Beckmann distribution in the Torrance-Sparrow microfacet model incorporates microscopic v-grooves of same widths with Gaussian distributed depths over the surface. This is equivalent to having a Gaussian distribution in the tangent space of angular normal deviations (θ_d) over the

surface.

$$\Theta_d \sim \mathcal{N}(\tan(\theta_d); 0, \sigma^2), \tag{B.4}$$

where Θ_d is a random variable for the angular deviation of the microscopic normal from the macroscopic normal, and σ is the roughness parameter.

Although Beckmann distribution is sufficiently simple for Monte Carlo integrators, it does not have good properties that allow analytic integration over multiple reflecting events. Therefore, we further simplify the model by making two assumptions.

1. We assume small angular deviations of microscopic normals from the macroscopic normal. Second-order approximation at $\theta_d = 0$ yields $\tan(\theta_d) \approx \theta_d$, which leads to a Gaussian half-vector distribution.

$$\tilde{\Theta}_d \sim \mathcal{N}(\theta_d; 0, \sigma^2). \tag{B.5}$$

Small angular deviations of microscopic normals also enable us to use, for an incident angle θ_i, a locally linear approximation for the Snell's law,

$$\theta_o = \sin^{-1}\left(\frac{n_1}{n_2}\sin\theta_i\right) - k\theta_d, \tag{B.6}$$

where

$$k(\theta_i) = \frac{\cos\theta_i}{\sqrt{\left(\frac{n_2}{n_1}\right)^2 - \sin^2\theta_i}}. \tag{B.7}$$

2. We follow Ward's approximation scheme in [War92], which considers the geometric masking factor and the Fresnel factor in the microfacet theory to counteract each other. Note that this implicitly makes half-vector distribution directly proportional to bidirectional scattering distribution function in the half-vector space.

From a single exocuticle layer, all the reflected light is contributed by each of

the $\text{tr}^{(2n+1)}\text{t}$ paths, and all the transmitted light is contributed by each of the $\text{tr}^{(2n)}\text{t}$ paths, where $n \in \mathbb{N}$, and t and r indicates transmission and reflection events respectively. Within each of the path, over the many reflections, the angular deviation of a ray from the ideal specular angle is proportional to the summation of all the angular deviations for each scattering event. Under our approximation scheme, since the angular-dependent geometric and Fresnel factors counteract each other, radiance that remains within a light path merely decays geometrically over each bounce. As for the two transmission events that sandwich all the reflection events, under locally linear approximation of Snell's law, they simply reduce to two additional angular deviations just like the reflection events. Thus, for a $\text{tr}^{(n)}\text{t}$ path, we can write down a random variable as its effective angular deviation of microscopic normal from macroscopic normal,

$$\tilde{\Theta}_{\text{d}}^{(n)} = k\tilde{\Theta}_{\text{d},0} + \sum_{i=1}^{n} \tilde{\Theta}_{\text{d},i} + k\tilde{\Theta}_{\text{d},n+1}, \tag{B.8}$$

where $\tilde{\Theta}_{\text{d},0}$, $\tilde{\Theta}_{\text{d},1}$, $\cdots$, $\tilde{\Theta}_{\text{d},n+1}$ are all independent and identically distributed Gaussian random variables as discussed above for $\tilde{\Theta}_{\text{d}}$. This gives

$$\tilde{\Theta}_{\text{d}}^{(n)} \sim \mathcal{N}\left(\theta_{\text{d}}; 0, (2k(\theta_{\text{i}})^2 + n)\sigma^2\right). \tag{B.9}$$

We can now form the collective half-vector distribution by summing up the distributions of effective angular deviations for each path, and weighted them by the probability a ray of light falls into that path.

$$\tilde{\Theta}_{\text{d,r}} \sim R\mathcal{N}(\theta_{\text{d}}; 0, \sigma^2) + (1-R)^2 \sum_{n=0}^{\infty} R^{2n+1}\mathcal{N}\left(\theta_{\text{d}}; 0, (2k(\theta_{\text{i}})^2 + 2n + 1)\sigma^2\right), \tag{B.10}$$

where R is an (averaged) effective reflectance. In the continuous limit of summation, the

formula becomes

$$\tilde{\Theta}_{d,r} \sim R\mathcal{N}(\theta_d; 0, \sigma^2) + (1-R)^2 \mathcal{N}\left(\theta_d; 0, (2k(\theta_i)^2 + N)\sigma^2)\right) \tag{B.11}$$

where N is a random variable under exponential distribution.

$$N \sim \exp(-\ln R). \tag{B.12}$$

The above formulation breaks down the cuticle effects into a surface term and a scattering term, providing novel phenomenological insights. While the surface term is just a normal distribution, the scattering term is more interesting in a way that it addresses the heavy tail in all the observed lobes, especially the specular R, TT and TRT lobes. Since the refractive index of a fur fiber is around 1.55, it can be shown that $|k(\theta_i)^2| < 0.5$, and that the exponential random variate N becomes prominent in most cases. For this scattering term, since it is a normal distribution with an exponentially distributed random variate as its variance, it becomes equivalent to a Laplacian random variable, as stated in [KKP12].

Finally, for l layers of cuticle scales, the effective half-vector distribution simply becomes a summation of l Laplace distributions, which is also a Laplace distribution. This result indicates that under humble microfacet normal deviations, we can use a Laplacian distribution to adequately approximate inter-reflection between cuticle scales. Therefore, when one requires a more accurate treatment for cuticle, according to B.11, we suggest using a Gaussian distribution to model the peak of the highlight, and a Laplacian distribution to model the tail of the lobe. Potentially, the simplest approach would be to use the mixture of a Gaussian and a Laplacian distribution to model the falloffs for all specular lobes.

Bibliography

[CH11]   Ellen Carrlee and Lauren Horelick. The alaska fur id project: A virtual resource for material identification. In *Objects Specialty Group Postprints*, volume 18. American Institute for Conservation of Historic and Artistic Works, 2011.

[Dav06]   AnthonyB. Davis. Effective propagation kernels in structured media with broad spatial correlations, illustration with large-scale transport of solar photons through cloudy atmospheres. In Frank Graziani, editor, *Computational Methods in Transport*, volume 48 of *Lecture Notes in Computational Science and Engineering*, pages 85–140. Springer Berlin Heidelberg, 2006.

[dFH+11]   Eugene d'Eon, Guillaume Francois, Martin Hill, Joe Letteri, and Jean-Marie Aubry. An energy-conserving hair reflectance model. In *Proceedings of the Twenty-second Eurographics Conference on Rendering*, EGSR '11, pages 1181–1187, Aire-la-Ville, Switzerland, Switzerland, 2011. Eurographics Association.

[DK04a]   Douglas W Deedrick and Sandra L Koch. Microscopy of hair part 1: A practical guide and manual for human hairs. *Forensics Science Communication*, 2004.

[DK04b]   Douglas W Deedrick and Sandra L Koch. Microscopy of hair part ii: a practical guide and manual for animal hairs. *Forensics Science Communication*, 2004.

[DLR+09]   Craig Donner, Jason Lawrence, Ravi Ramamoorthi, Toshiya Hachisuka, Henrik Wann Jensen, and Shree Nayar. An empirical bssrdf model. *ACM Trans. Graph.*, 28(3):30:1–30:10, July 2009.

[DM97]   Paul E. Debevec and Jitendra Malik. Recovering high dynamic range radiance maps from photographs. In *Proceedings of the 24th Annual Conference on Computer Graphics and Interactive Techniques*, SIGGRAPH '97, pages 369–378, New York, NY, USA, 1997. ACM Press/Addison-Wesley Publishing Co.

[dMH13]   Eugene d'Eon, Steve Marschner, and Johannes Hanika. Importance sampling for physically-based hair fiber models. In *SIGGRAPH Asia 2013 Technical Briefs*, page 25. ACM, 2013.

[dMH14]   Eugene d'Eon, Steve Marschner, and Johannes Hanika. A fiber scattering model with non-separable lobes. In *ACM SIGGRAPH 2014 Talks*, SIGGRAPH '14, pages 46:1–46:1, New York, NY, USA, 2014. ACM.

[DU03]   Michael W. Davidson and The Florida State University. Darkfield microscopy image gallery – mink fur., 2003.

[GGKGJ11]   Antonn Galatk, Jan Galatk, Zdislav Krul, and Antonn Galatk Jr. Furskin identification, 2011.

[Has88]   Ken Hashimoto. The structure of human hair. *Clinics in Dermatology*, 6(4):7–21, 1988.

[HG41]   Louis G Henyey and Jesse Leonard Greenstein. Diffuse radiation in the galaxy. *The Astrophysical Journal*, 93:70–83, 1941.

[HLLS11]   Bodo D. Wilts Hein L. Leertouwer and Doekele G. Stavenga. Refractive index and dispersion of butterfly chitin and bird keratin measured by polarizing interference microscopy. *Opt. Express*, 19(24):24061–24066, Nov 2011.

[HR12]   Christophe Hery and Ravi Ramamoorthi. Importance sampling of reflection from hair fibers. *Journal of Computer Graphics Techniques (JCGT)*, 1(1):1–17, 2012.

[Jak10]   Wenzel Jakob. Mitsuba renderer, 2010. http://www.mitsuba-renderer.org.

[KK89]   J. T. Kajiya and T. L. Kay. Rendering fur with three dimensional textures. In *Proceedings of the 16th Annual Conference on Computer Graphics and Interactive Techniques*, SIGGRAPH '89, pages 271–280, New York, NY, USA, 1989. ACM.

[KKP12]   Samuel Kotz, Tomasz Kozubowski, and Krzysztof Podgorski. *The Laplace distribution and generalizations: a revisit with applications to communications, economics, engineering, and finance*, chapter 2. Springer Science & Business Media, 2012.

[KVVU09]   Aleksey Kharin, Babu Varghese, Rieko Verhagen, and Natallia Uzunbajakava. Optical properties of the medulla and the cortex of human scalp hair. *Journal of Biomedical Optics*, 14(2):024035–024035–7, 2009.

[MJC⁺03]   Stephen R. Marschner, Henrik Wann Jensen, Mike Cammarano, Steve Worley, and Pat Hanrahan. Light scattering from human hair fibers. In *ACM SIGGRAPH 2003 Papers*, SIGGRAPH '03, pages 780–791, New York, NY, USA, 2003. ACM.

[NSA⁺02a] Shinobu Nagase, Satoshi Shibuichi, Kenichi Ando, Emiko Kariya, and Naoki Satoh. Influence of internal structures of hair fiber on hair appearance. ii. consideration of the visual perception mechanism of hair appearance. *J. Soc. Cosmet. Chem.*, 53:387–402, 2002.

[NSA⁺02b] Shinobu Nagase, Satoshi Shibuichi, Kenichi Andoa, Emiko Kariya, and Naoki Satoh. Influence of internal structures of hair fiber on hair appearance. i. light scattering from the porous structure of the medulla of human hair. *J. Soc. Cosmet. Chem.*, 53:89–100, 2002.

[OYM⁺03] Masayuki Okamoto, Ryoko Yakawa, Akira Mamada, Shigeto Inoue, Shinobu Nagase, Satoshi Shibuichi, Emiklo Kariya, and Naoki Satoh. The optical properties of human hair iii. generation of light-scattering factors in hair cuticles and the influence on hair shine. *J. Soc. Cosmet. Chem.*, 54:353–366, 2003.

[Rob12]   Clarence R. Robbins. *Chemical and Physical Behavior of Human Hair*, chapter 2. Springer-Verlag Berlin Heidelberg, 2012.

[SGF77a]   Robert F. Stamm, Mario L. Garcia, and Judith J. Fuchs. The optical properties of human hair i. fundamental considerations and goniophotometer curves. *J. Soc. Cosmet. Chem.*, 28:571–599, 1977.

[SGF77b]   Robert F. Stamm, Mario L. Garcia, and Judith J. Fuchs. The optical properties of human hair ii. the luster of hair fibers. *J. Soc. Cosmet. Chem.*, 28:601–609, 1977.

[SMKK06]   Hajime Sato, Hideaki Matsuda, Satoshi Kubota, and Koichi Kawano. Statistical comparison of dog and cat guard hairs using numerical morphology. *Forensic Science International*, 158(23):94 – 103, 2006.

[SPJT10]   Iman Sadeghi, Heather Pritchett, Henrik Wann Jensen, and Rasmus Tamstorf. An artist friendly hair shading system. *ACM Transactions on Graphics (TOG)*, 29(4):56, 2010.

[Sto60]   George G Stokes. On the intensity of the light reflected from or transmitted through a pile of plates. *Proceedings of the Royal Society of London*, 11:545–556, 1860.

[War92]   Gregory J. Ward. Measuring and modeling anisotropic reflection. *SIGGRAPH Comput. Graph.*, 26(2):265–272, July 1992.

[WMLT07]   Bruce Walter, Stephen R. Marschner, Hongsong Li, and Kenneth E. Tor-
           rance. Microfacet models for refraction through rough surfaces. In *Pro-
           ceedings of the 18th Eurographics Conference on Rendering Techniques*,
           EGSR'07, pages 195–206, Aire-la-Ville, Switzerland, Switzerland, 2007.
           Eurographics Association.

[ZRL+09]   Arno Zinke, Martin Rump, Tomás Lay, Andreas Weber, Anton Andriyenko,
           and Reinhard Klein. A practical approach for photometric acquisition of
           hair color. In *ACM SIGGRAPH Asia 2009 Papers*, SIGGRAPH Asia '09,
           pages 165:1–165:9, New York, NY, USA, 2009. ACM.

[ZW07]   Arno Zinke and Andreas Weber. Light scattering from filaments. *Visual-
           ization and Computer Graphics, IEEE Transactions on*, 13(2):342–356,
           2007.

[ZYWK08]   Arno Zinke, Cem Yuksel, Andreas Weber, and John Keyser. Dual scattering
           approximation for fast multiple scattering in hair. In *ACM SIGGRAPH
           2008 Papers*, SIGGRAPH '08, pages 32:1–32:10, New York, NY, USA,
           2008. ACM.